N-body simulations of the exocomets of the PDS 70 system

Alexandra Stockwell Murphy

Division of Astrophysics
Department of Physics

Lund University

2026–EXA267

Degree project of 60 higher education credits
June 2026

Supervisors: Jens Hoeijmakers & Anders Johansen & Aline Novais

Division of Astrophysics
Department of Physics
Box 118
SE-221 00 Lund
Sweden

ABSTRACT

Comets in the Solar System are time capsules; their composition tells us what materials were present in our system millions of years ago. We now know that other systems also show cometary activity, called exocomets. As we refine the methodology for detecting exocomets and our instruments improve, more and more of these systems will be found. PDS 70 , the first system with confirmed accreting protoplanets, may be one such exocomet-hosting system.

By analysing spectroscopic data of the PDS 70 star, Lund researchers detected absorption features in neutral sodium that vary in radial velocity over time. Similar variable absorption lines are observed in the confirmed exocomet-hosting system β Pictoris , where they are interpreted as gas clouds released by star-grazing exocomets crossing the line of sight to the star at different velocities.

In β Pictoris, it is known that the massive planets play a crucial role in creating these exocomets and stirring up planetesimals in the disc, scattering them inwards and so close to the star that they become star-grazing. However, while the innermost planet in β Pictoris is at less than 3 AU from the star, the confirmed innermost planet in PDS 70 orbits at about 21 AU. Therefore, it is not clear that these far-out planets could even be sufficient to produce the observed exocomets.

In this project, I use N-body simulations to study the dynamics of the planets and planetesimals in the disc of PDS 70. While doing this, I realised that the unconstrained masses of the two directly imaged planets played an important role in the system's stability, and I worked on finding the most stable configurations for the two-planet system. I show that the system becomes unstable and planets can become unbound if PDS 70 b (the inner planet) is more massive than PDS 70 c (the outer planet). In particular, in the cases where $7 \leq M_b \leq 11 M_{\mathrm{Jup}}$, if $M_b - M_c \geq 6 M_{\mathrm{Jup}}$, 100% of the simulations performed led to unstable solutions.

I also include the unconfirmed third planet in this stability analysis. I show that it is unlikely that this proposed inner planet (PDS 70 d) is more massive than 1 M_{Jup}.

I then simulate an outer disc of planetesimals (> 54 AU) and track how often they cross the gap carved by the planets into the inner disc (< 18 AU). I show that in the final 1 Myr of a 5 Myr simulation, an average of 0.45% of particles cross the gap in the 2-planet case and 2.4% do so in the 3-planet scenario. This shows that it is dynamically feasible for planetesimals to cross the gap.

The final stages of this project were dedicated to understanding the particle dynamics once they reach the inner disc and whether particles reach close enough to the star to be considered star-grazing (periastron distances below 0.4 AU). Here, I include the effects of gas drag and find that it has little influence on the rates at which exocomets are created. However, its effect scales with the size of the planetesimals and 1 km radius objects are less likely to become star-grazing than 100 km radius objects. The gas friction and radiation heating in the inner disc can also lead to ablation (the destruction of planetesimals). I find that ablation is very effective, and most planetesimals that become star-grazers are destroyed within a few orbits, depositing their water content in the inner disc. On the other hand, particles that reach high inclinations before reaching the ablation zone can survive for hundreds to thousands more orbits.

Together, these results support the interpretation of PDS 70 as a plausible exocomet-hosting system and provide insight into how young multi-planet systems can drive cometary material toward their host stars.

Acknowledgements

I would like to express my sincerest gratitude to my main supervisor, Jens, for proposing such an engaging thesis topic with so many dimensions to explore, and for helping me find my way whenever I felt lost. I am deeply thankful for my co-supervisor Aline, for her constant guidance, encouragement, and for always reminding me to believe in myself. I would also like to thank my co-supervisor Anders, from whom I learned a great deal and whose insights were invaluable in shaping the final project.

To the rest of the Lund Exoplanet Atmospheres group, thank you for the advice, discussions, and support shared in our meetings over the last year and a half. I am especially grateful to Bibi for bringing me along to Chile and introducing me to the world of observations, which I am excited to continue exploring during my PhD.

I would also like to thank my friends and colleagues at the Department of Astrophysics for creating such a welcoming and supportive work environment. I am especially grateful to my fellow master's students and office mates, whose kindness, care, and friendship made these two years truly memorable.

Last but not least, I am deeply grateful to my family for their continuous support throughout my educational journey, and to Lucas, for bringing balance to my chaotic life and supporting me in every possible way.

Popular Science Summary

Comets in our Solar System are time capsules packed with material from the early stages of planet formation. In recent years, astronomers have detected other systems with signs of comet-like bodies, known as exocomets. One system with hints of exocomet activity is PDS 70 , the first known system where two giant planets are still actively forming.

Exocomets are detected when the object's tail, primarily composed of gas, covers the star as it passes in front of it. When this happens, we observe absorption lines at different radial velocities for each passing comet, as they transit from different directions and at different speeds. Similar signals have been found in other systems, namely, β Pictoris , where exocomets have been confirmed. Much like Jupiter shapes the orbits of Solar System comets, giant planets in other systems, like β Pictoris or PDS 70 , will play a large role in scattering icy bodies towards the star, creating exocomets that we can detect from Earth.

However, the planets in PDS 70 orbit much further than Jupiter or β Pictoris b, making it unclear whether they can drive the same process. To investigate this, I simulate the motions of planets and thousands of small comet-sized particles (planetesimals) located in a disc around the star to understand how their motions evolve over time. The simulations show that the system's stability strongly depends on the masses of the planets, which are not well-defined. If the innermost planet is more massive than the outer one, the system becomes very unstable and breaks down. If I include a third planet in the system, which has been proposed to exist but is not yet confirmed, the masses of all three planets become constrained to no more than one to a few Jupiter masses.

By studying a disc of planetesimals, I found that a small percentage of particles can reach the inner regions and even graze the star. Many of these particles approach the star so closely that they are completely destroyed by heat and gas friction, depositing all their water content. Other particles are able to reach higher inclinations, which means they interact less with the gas disc around the star and can survive for more orbits. These are likely the exocomet candidates.

Overall, this work shows that even planets orbiting far from their host star can send comet-like bodies into inner regions, making PDS 70 a strong candidate for hosting exocomets. It also shows that exocomets can deliver water into the inner disc.

POPULÄRVETENSKAPLIG BESKRIVNING

Kometer i vårt solsystem fungerar som tidskapslar fyllda med material från de tidiga stadierna av planetbildning. Under de senaste åren har astronomer upptäckt andra planetsystem med tecken på kometliknande objekt, så kallade exokometer. Ett system med möjliga spår av exokometaktivitet är PDS 70 , det första kända systemet där två jätteplaneter fortfarande håller på att bildas.

Exokometer upptäcks när objektets svans, som huvudsakligen består av gas, passerar framför stjärnan och delvis täcker dess ljus. Eftersom kometerna passerar framför stjärnan från olika riktningar och med olika hastigheter ser vi absorptionslinjer med olika radialhastigheter för varje förbipasserande komet. Liknande signaler har hittats i andra system, framför allt β Pictoris , där exokometer har bekräftats. Precis som Jupiter påverkar banorna hos kometer i vårt eget solsystem spelar jätteplaneter i andra system, som β Pictoris och PDS 70 , en viktig roll genom att sprida isrika objekt in mot stjärnan och skapa exokometer som vi kan upptäcka från jorden.

Planeterna i PDS 70 kretsar dock mycket längre från sin stjärna än både Jupiter och β Pictoris b, vilket gör det oklart om de verkligen kan driva samma process. För att undersöka detta simulerar jag rörelserna hos planeter och tusentals små kometstora partiklar, så kallade planetesimaler, i en skiva runt stjärnan för att förstå hur deras banor utvecklas över tid. Simulationerna visar att systemets stabilitet är starkt beroende av planeternas massor, vilka inte är väl bestämda. Om den innersta planeten är mer massiv än den yttre blir systemet mycket instabilt och kan brytas sönder. Om jag inkluderar en tredje planet i systemet, som har föreslagits men ännu inte bekräftats, begränsas massorna hos alla tre planeterna till högst omkring en till några Jupiter-massor.

Genom att studera en skiva av planetesimaler fann jag att en liten andel av partiklarna kan nå de inre delarna av systemet och till och med passera mycket nära stjärnan. Många av dessa partiklar kommer så nära att de förstörs helt av upphettning och gasfriktion och därmed avger allt sitt vatteninnehåll. Andra partiklar når högre lutningar i sina banor, vilket innebär att de växelverkar mindre med gasskivan runt stjärnan och därför kan överleva under fler omlopp. Det är sannolikt dessa objekt som utgör kandidaterna till exokometer.

Sammantaget visar detta arbete att även planeter som kretsar långt från sin värdstjärna kan skicka kometliknande objekt in mot de inre delarna av planetsystemet, vilket gör PDS 70 till en stark kandidat för att hysa exokometer. Resultaten visar också att exokometer kan transportera vatten till den inre skivan.

CONTENTS

CHAPTER 1

INTRODUCTION

Comets in our Solar System are valuable objects to study, as they carry essential information from the early history of the Solar System (Whipple 1950; Blum et al. 2022). Their chemical composition sheds light on the processes that shaped the Solar System during ongoing planet formation. Recently, several other systems have shown evidence of cometary activity. These so-called exocomets, which orbit other stars, provide a unique opportunity to study planet formation in other systems.

Exocomets can be detected indirectly, by observing absorption features in stellar spectra that are Doppler shifted relative to the star, or dips in the flux from the star as the exocometary tail covers its surface. As in our own Solar System, these objects could be byproducts of planet formation, and their orbits can reveal the dynamical structure of their host systems, as well as the influence of planets that perturb their orbits.

This work will focus on one particular system, PDS 70, which is home to at least two giant forming planets and is likely to host exocomets.

1.1 THE PDS 70 SYSTEM

PDS 70 is a T Tauri K7-type star of radius 1.26 ± 0.15 $R_\odot$ (Keppler, Benisty, et al. 2018) and mass 0.76 ± 0.02 $M_\odot$ (Müller et al. 2018), located at a distance to our Sun of 113 ± 0.5 pc (Gaia Collaboration et al. 2018) in the Scorpius-Centaurus association (Pecaut et al. 2016). It hosts two forming gas giants, PDS 70 b and PDS 70 c, at orbits of $\sim$ 21 AU and $\sim$ 34 AU from the star, respectively, which have cleared a gap between an inner disc (up to $\sim$ 18 AU) and an outer disc (from $54 - 87$ AU) (Benisty et al. 2021). The system is 51.7 ± 0.01 degrees inclined with respect to the plane of the sky (Keppler, Benisty, et al. 2018). The two planets, observed in 2018 (Keppler, Benisty, et al. 2018) and 2019 (Haffert et al. 2019), respectively, were directly imaged, which does not allow for strong constraints on their masses (see section 1.3.1). These could range anywhere from $\sim 1 M_{\mathrm{Jup}}$ up to $\sim 12 M_{\mathrm{Jup}}$ (Wang et al. 2021). The system is roughly 5.4 million years old (Keppler, Benisty, et al. 2018) and is one of the only systems with detected planets embedded in a protoplanetary disc. This makes it an ideal laboratory where planet formation theories can be put to the test against observations.

Recent observations have detected a point-like source at approximately 13 AU moving at Keplerian speed, observed across several epochs (Christiaens et al. 2024; Hammond et al. 2025). While this could be a third protoplanet, there is not enough evidence to rule out the possibility of it being a dust clump. Due to the unclear nature of the source, I explore both scenarios in this thesis (the two- and three-planet cases).

Analysis of archival HARPS (High Accuracy Radial velocity Planet Searcher) data of the PDS 70 star has shown the presence of variable absorption lines of neutral sodium (Novais et al. 2025 - in review). That is, absorption lines embedded in the broad stellar line, at varying radial velocities over time (see figure 1.1). The origin of this variability and high Doppler shifts is proposed to be due to exocomets transiting the star. Since the absorption lines are Doppler shifted, the source must be moving with respect to

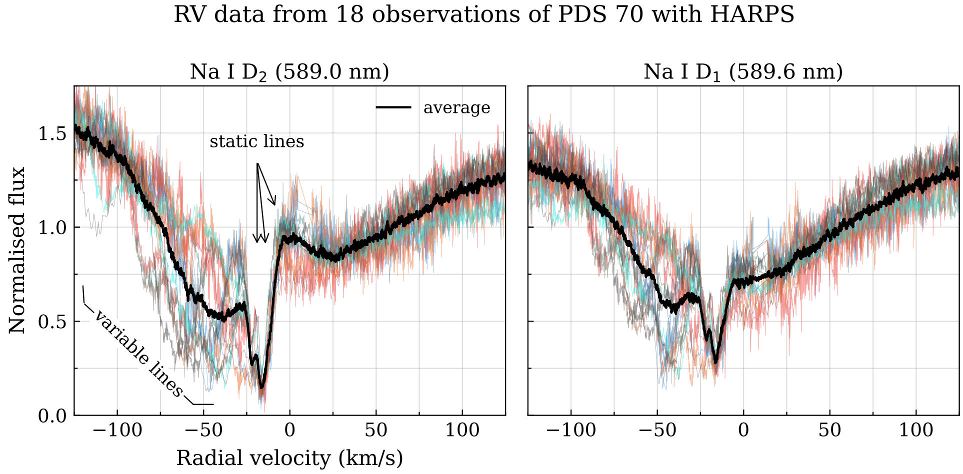

Figure 1.1: Variable absorption lines around the sodium doublet, attributed to exocomet activity. Each coloured curve represents the computed radial velocities for one night of observation. The black line is the average over all nights. Besides the variable features, some lines do not vary over time; for example, in the first panel, one can see an emission line around RV = 0 km/s, potentially due to stellar accretion, and in both panels, two partially blended, deep, non-varying absorption lines. The line at around 16 km/s could be from the ISM (interstellar medium), but due to the blendedness, this remains unconfirmed.

the star. Similar features have been observed in a small number of systems (Iglesias et al. 2025), notably, β Pictoris (Ferlet et al. 1987), where exocomets have been confirmed, and are now a common marker for exocomet activity.
The lines seen in PDS 70 are highly blue-shifted (see figure 1.1), which may also be attributed to disc-winds, an outflow of gas and dust from the protoplanetary disc near the protostar. However, a few arguments disfavour this explanation. Firstly, the variations in PDS 70 can be seen as fast as in a few hours, which is unlikely in disc winds (Alencar et al. 2000; Edwards et al. 2006; Espaillat et al. 2021). Secondly, the calculated column densities of sodium do not match those of disc winds. The column density of a species is the number of atoms of that species along the line of sight, expressed in units of particles per area. Comparing the sodium column density from disc winds to that measured from PDS 70 observations reveals that the latter show values one to two orders of magnitude higher (Novais et al. 2025). This means that, although wind effects cannot be ruled out, they do not fully explain the variable absorption either. Since only a portion of the star is covered as the cloud of gas making up the exocomet tail transits, it can be concluded that the gas is clumpy (Lagrange-Henri et al. 1989). This spatial confinement is a robust argument that makes exocomets the most likely source (Kiefer, Etangs, et al. 2014).

Another interesting finding in this system, based on data from JWST (James Webb Space Telescope), is the detection of water emission in the inner system, around 0.05 AU (Perotti et al. 2023). This raises several questions, as there is no clear explanation for the origin of this water. Formation in situ is one possibility (Perotti et al. 2023); however, another solution could be the transport of ice by small dust particles that can cross the depleted, but not empty, planet-carved gap (Pinilla et al. 2024). This transport could also be done by other means, such as via planetesimals that cross the gap from the outer system, similar to our own solar system, as proposed by Novais et al. 2025.

1.2 Defining and detecting exocomets

Comets in our solar system (Whipple 1950; Blum et al. 2022) are small bodies composed of volatiles (ices, with low condensation temperatures) and refractory materials (dust, with high condensation temperatures) that orbit the Sun. These objects are typically tens to hundreds of kilometres in diameter. As they approach the Sun, the volatiles sublimate (outgassing) due to their low condensation temperatures, carrying small rocky particles with them and creating distinct tails of gas and dust escaping from the nucleus. Under extreme heating, some refractory materials may also sublimate or fragment, contributing to the gas and dust tail. When such an object, with signs of sublimation and a tail of gas and dust, is detected orbiting another star, it is referred to as an exocomet.

There are two main methods of detecting exocomets. The first is via spectroscopic observations of the gas in the exocometary tail as it transits the star across the line of sight, similar to what is proposed in PDS 70 (Novais et al. 2025). This transit is observed as absorption lines in the stellar spectra, which vary in radial velocity on a short period of a few days. These lines can belong to several different species, the most typical being Calcium, Sodium, and Iron. The first evidence of exocomets was found in the β Pictoris system through spectroscopic observations of time-variable Ca II K and H absorption lines (Ferlet et al. 1987). Today, about 30 systems have been reported to show this type of variability (Iglesias et al. 2025). However, these features are stochastic, and the frequency of transits and the transiting objects' orbits are unpredictable from observations.

The second method of detection is via photometry, where a dip in the star's light curve is measured. This transit is usually asymmetric and attributed to the passing of an exocomet with a dust tail (e.g. Boyajian et al. 2016; Rappaport et al. 2018; Zieba et al. 2019). The ingress (the start of the transit) leads to a sharp dip in the light curve, as the dense nucleus of the comet passes first and blocks part of the starlight. The egress (when the comet moves off the stellar disc) is longer, and the brightness gradually increases during this time, since, after the nucleus has left the stellar disc, the trailing tail of dust continues to obscure a smaller amount of light.

There are two systems where exocomets have been observed using both of these methods - β Pictoris (Ferlet et al. 1987, Zieba et al. 2019) and HD 172555 (Kiefer, Lecavelier Des Etangs, et al. 2014, Bendahan-West et al. 2025, Grady et al. 2018) - and exocomets are considered "confirmed". Other cases where there are few observations are candidate exocomet-hosting systems (Iglesias et al. 2025). Another important property that can help define an exocomet detection is that transiting exocomets are spatially confined. This implies having a fill-fraction below unity (modelled from the line depths), meaning the star is only partially covered by the cloud of gas and dust.

Although these observational signatures can provide strong evidence for exocomets, such events are difficult to detect and monitor, resulting in relatively limited datasets. Therefore, simulations serve as a tool for testing formation and dynamical scenarios and making predictions. For example, in β Pictoris , the two families of exocomets found in Kiefer, Etangs, et al. 2014 were later confirmed through simulations (Jaworska et al. 2026). Before the planets were even discovered, it was suggested that the exocomets were in mean motion resonance with a planet on an eccentric orbit (Beust and Morbidelli 1996). This model, and revisited versions of it (Beust, Milli, et al. 2024), explain why the β Pictoris exocomets are preferentially redshifted, and how their orbits tend to become aligned with that of the inner planet (Jaworska et al. 2026).

1.3 Observations

PDS 70 is one of the only observed systems with confirmed protoplanets. In this section, I will highlight some tools and methods for observing exoplanets relevant to this thesis and the PDS 70 system in general.

1.3.1 Direct Imaging

Direct imaging is a technique for detecting and characterising exoplanets which relies on the collection of photons emitted or reflected by a planet. With the current technology, this method has been most successful with young planets, which are hot and bright, on wide orbits, where the angular separation between the star and the planet is large enough to be resolved.

One of the main challenges in directly imaging exoplanets is the contrast, that is, the ratio between the planet's brightness and the star's. One way to increase the contrast is to block the starlight. This can be done using a coronagraph (ground- and space-based observations) or a starshade (space-based observations). This is often accompanied by the use of adaptive optics (AO) to instantaneously correct for atmospheric distortions using deformable mirrors (Davies et al. 2012). Another way to achieve higher contrasts is by choosing appropriate wavelengths to observe. While the peak in emission for a star is visible wavelengths, the black body curves of planets peak in the near-infrared to the mid-infrared. This is especially true for young, self-luminous planets. For this reason, direct imaging uses near- to mid-infrared light, providing contrasts several orders of magnitude higher.

Once a planet is detected through direct imaging, its mass can be indirectly determined. Mass estimates are made by using evolutionary models to convert luminosity to mass. However, these models are not well calibrated at young ages and include various assumptions on the planet's formation. Namely, the assumed gas-accretion phase during which the exoplanet atmosphere forms will have a large impact on the final planetary mass (Chauvin 2024). Combining this with the uncertainty on the system's age, it becomes difficult to determine the masses of directly imaged planets, which explains the large uncertainty range for the PDS 70 planet masses.

1.3.2 Spectroscopy

Spectroscopy is one of the most used techniques in astronomy, where incoming light is decomposed into a spectrum. Studying the spectrum of a star, for example, can give insights into the stellar temperature, rotation, and chemical composition. Similar conclusions can be made when using spectroscopy to study a planet's atmosphere. For example, in PDS 70 , the presence of an Hα emission line in spatially-resolved spectra of the planets was an indication of ongoing planetary accretion (Haffert et al. 2019; Hashimoto, Aoyama, et al. 2020). The Hα line is often associated with accretion, since it is produced when infalling material crashes onto the planet's atmosphere, generating a shock, heating the gas to several thousand Kelvin, and then emitting Hα as it cools and recombines (Chen et al. 2022). From the corrected luminosity and linewidth of these emission lines, Hashimoto, Aoyama, et al. 2020 find a mass accretion rate above $5 \times 10^{-7}\,\mathrm{M_{Jup}/yr}$ for PDS 70 b, which is an order of magnitude higher than the stellar accretion rate, indicating active disc feeding.

By measuring shifts in stellar absorption-line positions, one can determine the star's radial velocity using the Doppler effect. This consists of a shift in wavelength of an observed spectral line due to the motion of an object away from or towards the observer. The radial velocity method can be used to detect exoplanets around a star due to the motion of the bodies around the common centre of mass (the barycentre). This is only possible in the configurations where the planet's orbit is aligned such that it moves away from us, causing a redshifted line, or towards us, causing a blueshifted line.

HARPS, the High Accuracy Radial velocity Planet Searcher, is a high-resolution spectrograph mounted on the 3.6-m ESO telescope at La Silla Observatory (Mayor et al. 2003). Spectra taken in 2018 using HARPS show variable absorption lines around the Na I D lines in the spectra of PDS 70 , attributed to exocomet activity (Novais et al. 2025). These can be seen in figure 1.1. This is another use of the radial velocity method, where a cloud of gas can show blue or redshifted absorption lines depending on whether it is receding from or approaching us, relative to the star.

1.4 Observed properties of PDS 70

Observations of PDS 70 have shown the presence of a large cavity in both dust (Hashimoto, Dong, et al. 2012; Dong et al. 2012) and gas (Keppler, Teague, et al. 2019).

Details of these structures have been unveiled in observations with ALMA, the Atacama Large Millimetre/Submillimetre Array, which uses longer wavelengths to probe dense star-forming regions composed of gas and dust. In the case of PDS 70 , observations with ALMA have shown a ring of dust that peaks in brightness at $\sim$ 74 AU (Keppler, Teague, et al. 2019). This peak is located in the northwest, which points to a dust accumulation that is not only radially dependent but also azimuthal (Doi et al. 2024). Moreover,

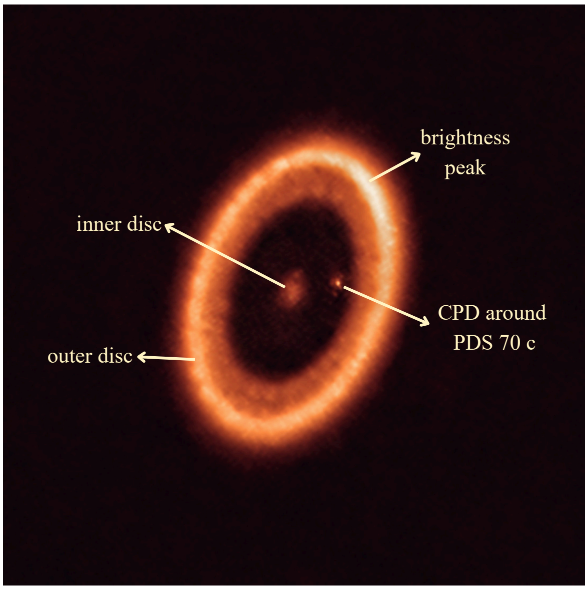

Figure 1.2: Image of the PDS 70 system taken with the Atacama Large Millimeter/submillimeter Array (ALMA). The brightness peak in the northwest is visible, as well as the CPD around planet c. Modified from ALMA (ESO/NAOJ/NRAO)/Benisty et al.

ALMA has helped identify a circumplanetary disc (CPD) around PDS 70 c (Benisty et al. 2021), the most compelling evidence for a CPD around an accreting planet yet. A CPD forms when material is captured by a planet and settles into an orbit around it (see section 2.2.1 for more). No CPD is detected around planet b, although simulations show that CPDs are theoretically expected to form around both planets (Toci et al. 2020). One possibility for the non-detection of a CPD around PDS 70 b is that the Hill radius of this planet is much smaller, due to it being at a smaller separation (see equation 2.8), making it harder to grow a CPD. Even if particles become trapped in the Hill sphere, the CPD would be hard to resolve. Another possible explanation is the trapping of larger grains by the outer planet, so that the flow of material across the gap is insufficient to accumulate material around PDS 70 b. In Pinilla et al. 2024, it was demonstrated that only small grains ($< 0.1\mu$m) can be carried with the gas across the gap created by the planets, and it could be that some of the material that could make its way towards the inner planet gets swept up by PDS 70 c. The CPD and the brightness peak are shown in figure 1.2.

1.5 The purpose and structure of this work

The quintessential exocomet-hosting system β Pictoris has been studied extensively, and N-body simulations of this system have shown that its two gas giants, especially the innermost planet at $\sim$ 3 AU, play a large role in scattering planetesimals (Beust, Milli, et al. 2024; Jaworska et al. 2026). In PDS 70, the innermost (confirmed) planet is located much further out, at about 21 AU. The question then arises whether it is even feasible for planetesimals created in the outer disc, $>$ 54 AU, to be scattered to the inner disc at 18 AU and even further inwards towards the star, eventually becoming exocomets. Moreover, due to the inclination of PDS 70 with respect to our line of sight, for exocomets to be observed as transits, the planetesimals must be excited onto inclined and eccentric orbits. I explore these questions through N-body simulations using the Python implementation of the REBOUND N-body integrator (Rein and Liu 2012).

The rest of this work is divided into four sections. In chapter 2, I give some context to the theory relevant to this project and necessary to understand the results. I will begin by exploring some key aspects of protoplanetary discs and their structure, introduce the two- and three-body problems, and conclude by discussing some of the effects gas has on planetesimals.

In chapter 3, I describe the methods used in this work. Namely, the use of REBOUND and the extension package REBOUNDX, and the setup of the three types of simulations performed - stability testing, simulating particles in the outer disc, and simulating particles in the inner disc.

The results are presented and discussed in chapter 4 in sections corresponding to the three types of simulations performed. In section 4.1, the influence of planetary mass on the stability of a two- and three-planet system is shown. In section 4.2, the results from the outer disc simulations are presented, including the rates at which particles cross from the outer to the inner disc. In section 4.3, I show the results from the inner disc simulations, namely, the influence of the gas drag force and the effect of ablation on the destruction of planetesimals.

Chapter 2

Theoretical background

2.1 Protoplanetary discs

2.1.1 Disc structure

As interstellar gas gravitationally collapses to form a protostar, conservation of angular momentum implies that a portion of the infalling material experiences an increase in rotational velocity. This material settles into approximately Keplerian orbits around the central object, ultimately forming a circumstellar disc. This is the protoplanetary disc, composed of 99% gas (hydrogen and helium) and about 1% small dust particles (Williams et al. 2011). The radii of these discs can extend from tens to hundreds of AU (Vicente et al. 2005), and they are geometrically thin (their vertical thickness is much smaller than the distance to the star). Figure 2.1 shows a schematic of a protoplanetary disc.

The surface density, $\Sigma(R)$ of protoplanetary discs is commonly modelled as inversely proportional to the distance to the star, R, and truncated at a characteristic radius R_c (Andrews et al. 2011; Williams et al. 2011)

$$\Sigma(R) = \Sigma_0 \left(\frac{R}{R_c}\right)^{-1} \exp\left(-\frac{R}{R_c}\right). \tag{2.1}$$

Σ_0 is the characteristic surface density, evaluated at the characteristic radius R_c. It is a normalisation constant that scales with the mass of the disc such that $M_{\text{disc}} = 2\pi \int \Sigma(r) r dr$, giving $\Sigma_c \propto \frac{M_{\text{disc}}}{R_c^2}$. In the case of PDS 70 , Σ_0 set to $2.7\,\text{g/cm}^2$ such that the total disc gas mass is $0.003 M_\odot$, as done in Keppler, Benisty, et al. 2018, in agreement with the total disc mass derived in Dong et al. 2012. R_c, the characteristic radius at which the exponential decay truncates, is defined to be 40 AU to remain consistent with Keppler, Benisty, et al. 2018. It is within R_c that most of the gas mass of the disc is concentrated. We assume a density of zero up to $3.4 R_\odot$, the inferred truncation radius for PDS 70 (Thanathibodee et al. 2020). The truncation radius is the location in the disc where the stellar magnetic field is strong enough to disrupt the disc and lift material away from it. At the truncation radius, the magnetic pressure from the star balances the ram pressure (due to movement within a medium) and the gas pressure from the disc.

A vertically isothermal optically thin disc has a temperature profile given by $T(R) \propto R^{-1/2}$ (Kenyon et al. 1987). The disc temperature is mainly determined by stellar irradiation and the dissipation of potential energy as gas accretes. Later work has found that a disc that is optically thick towards the star has a proportionality closer to $T(R) \propto R^{-3/7}$ (Ida, Guillot, et al. 2016). This is based on heating that is mainly from infrared photons from the upper layers of the disc, which have absorbed radiation. Due to how the scale height relates to the temperature, the temperature's dependency on R causes the outer regions of the disc to flare vertically away from the midplane, compared to the regions close to the star. The scale

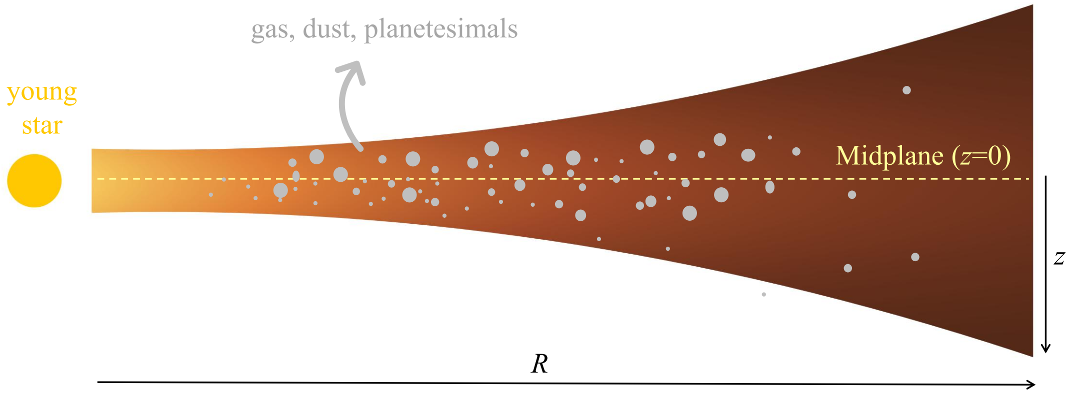

Figure 2.1: Example schematic of a protoplanetary disc.

height is the characteristic vertical thickness of a disc. It is the distance over which a quantity (such as density or pressure) falls by a factor of e. It can be computed as the ratio between the speed of sound and the Keplerian angular velocity

$$H = c_s/\Omega, \quad \text{where} \tag{2.2}$$

$$c_s = \left(\frac{k_B T}{\mu m_{\mathrm{H}}}\right)^{1/2} \text{ and } \Omega = \left(\frac{G M_*}{R^3}\right)^{1/2}. \tag{2.3}$$

Here, k_B is the Boltzmann constant, T is the temperature, μ is the mean molecular weight, m_{H} is the mass of the hydrogen atom and $R = \sqrt{x^2 + y^2 + z^2}$ with respect to the centre of mass frame. From equation 2.2 and equation 2.3, one can find that $H(R) \propto \sqrt{T(R)} R^{3/2}$. Using $T(R) \propto R^{-1/2}$, we obtain $H(R) \propto R^{5/4}$ (or $H(R) \propto R^{9/7}$, if using the temperature profile from Ida, Guillot, et al. 2016). This dependency on R means the disc thickness increases faster than the radius, giving the flared profile mentioned above and visible in figure 2.1 and figure 2.3.

The temperature profile of the PDS 70 disc is determined in Bae et al. 2019, starting with a simple irradiation formula that relates the temperature to the stellar luminosity and radius

$$T_{\mathrm{irr}} \propto \left(\frac{L_*}{R^2}\right)^{1/4}. \tag{2.4}$$

Assuming that, at each radius, the temperature is constant over height, z, they calculate the 3D gas density that satisfies vertical hydrostatic equilibrium. They then perform Monte Carlo calculations of dust grains coupled to gas to mimic heating from stellar light absorption and re-emission. The temperature is updated at every step, and the calculation is repeated until the average vertical temperature stabilises. The obtained power law after convergence is given in equation 2.5

$$T = 38 \left(\frac{R}{R_c}\right)^{-0.24} \mathrm{K}, \tag{2.5}$$

rewritten from Bae et al. 2019 in terms of the same characteristic radius as before, $R_c = 40$ AU. Once again, R is the distance to the star.

Moving away from the midplane, the density at a certain height z can be modelled as a Gaussian around the midplane (Deeg et al. 2018)

$$\rho(z) = \rho(z=0) \exp\left(\frac{-z^2}{2H^2}\right), \tag{2.6}$$

where $\rho(z=0) = \frac{\Sigma}{\sqrt{2\pi}H}$ is the midplane gas density, and H the scale height (length units), as defined in equation 2.2.

To account for the gas depletion in the gap, the gas density in this region (from 18 to 40 AU [1]) is decreased by a factor of 100. This choice is based on the simulations presented in Portilla-Revelo et al. 2023, which indicate that the gas density at the location of PDS 70 b is approximately 10^{-2} times that of the region exhibiting the highest emission.

A visual representation of the surface and midplane gas densities for the PDS 70 system, as a function of distance from the star, is shown in figure 2.2. The density given in equation 2.6 is plotted on an R-z grid and shown in figure 2.3.

2.1.2 T Tauri stars

At the centre of the protoplanetary disc is an accreting T Tauri star. The star T Tauri was discovered in 1852 by James Russell Hindt and stood out for its variation in brightness. It was later chosen as a prototype for a new class of stars, the T Tauri stars, defined by Joy 1945. These criteria were refined in 1962 (Herbig 1962) to be based solely on spectroscopic properties (Hydrogen lines, H and K lines in Ca II, fluorescent Fe I lines must be present in emission; if seen, S II, O I should be present in emission, and Li I in absorption). Stars with these criteria also show variable brightness and are associated with regions of high nebulosity (star-forming regions near or in dense molecular clouds). Ambartsumian 1947 was the first to suggest that T Tauri stars are young, and we now know that they are indeed pre-main-sequence stars, no more than a few million years old (Appenzeller et al. 1989). This means that they do not yet have the necessary core pressure and temperatures to commence hydrogen burning. A solar-mass T Tauri star will have a contraction timescale on the order of $\sim 10^7$ years, during which the star shrinks towards the main sequence. These stars are known for having strong stellar winds and UV and X-ray emission. This emission is highly variable and important, as it drives photoevaporation of the gas disc and can halt planet-disc interactions, such as migration (Do Ó et al. 2025).

T Tauri stars are still accreting gas from their surrounding disc and usually have masses below $3M_\odot$ (Appenzeller et al. 1989). The average accretion rate for a 1 Myr T Tauri star is in the order of 10^{-8} $M_\odot$/yr. This value declines with age as $\dot{M} \propto t^{-\eta}$, with η empirically determined to lie between 1.5 and 2.8 (Hartmann et al. 1998). The higher the η, the faster the disc is dispersed, and the faster the accretion comes to a halt. The large uncertainty in this parameter is due to the wide range of accretion rates at each age, the small age range of the sample, and uncertainties in the estimation of stellar ages and accretion luminosities. PDS 70 has a variable accretion rate in the order of $10^{-10}M_\odot$/yr (Thanathibodee et al. 2020), slightly higher than expected for its age, but relatively low compared to younger T-Tauri stars. This accretion rate is significant enough that the inner disc must somehow be resupplied with disc material (Thanathibodee et al. 2020), which could be done via dust leaking past the planets (Pinilla et al. 2024) or even planetesimals, as suggested in Novais et al. 2025.

[1]Note that the gap is assumed to be up to 40 AU in figure 2.2 but 54 AU is used in the simulations to set up the outer disc. Since both values can be found in the literature, this was done to remain conservative in the simulations. The further away from the outer planet the population of planetesimal begins, the fewer interactions occur, and the stronger the conclusions become. In the definition of the disc, we keep 40 AU since the temperature and density profiles were derived in the literature using this value.

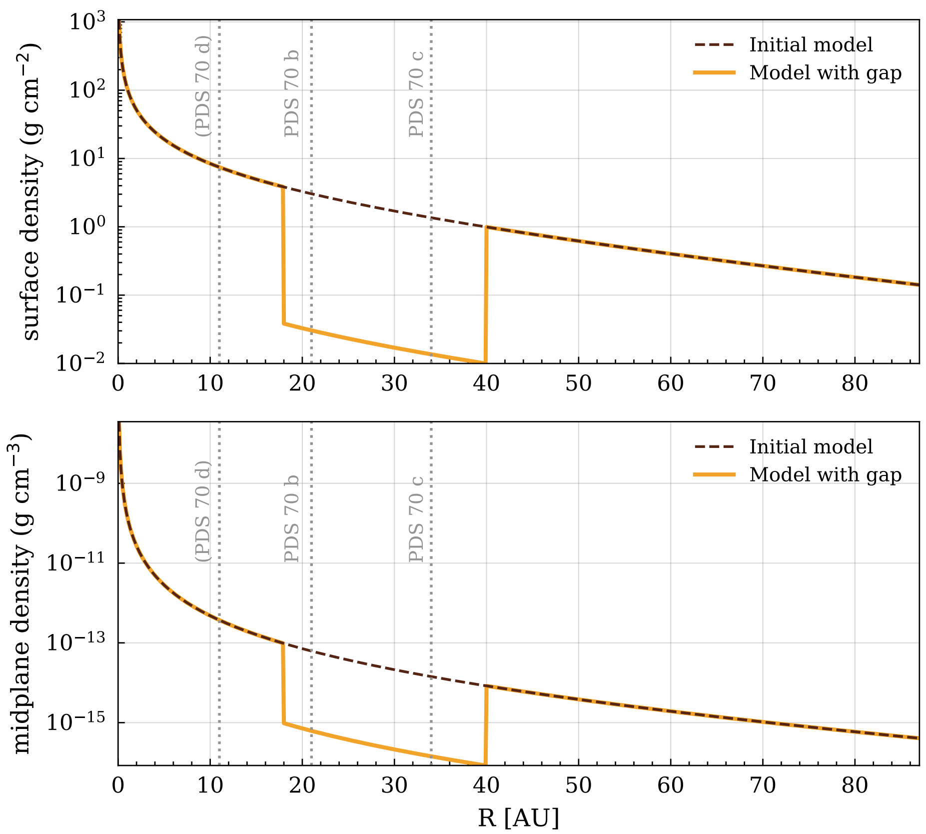

Figure 2.2: Profiles of the surface and midplane densities used to describe the PDS 70 system. The gap is created by reducing the density by a factor of 100 between 18 and 40 AU (Portilla-Revelo et al. 2023). The initial model, without the inclusion of the gap, is indicated as the brown dashed line. The planets are also shown at their semimajor axes, at 11, 21 and 34 AU respectively. The gas density decreases by several orders of magnitude with increasing distance, meaning it is most prominent close to the star.

2.1.3 Migration

As a protoplanet grows in mass, its gravitational interactions with the disc around it increase. The exchange of angular momentum between the planet and the disc forms spiral density waves in two directions. The inner spiral generates a positive torque and pulls the planet outwards, whereas the outer spiral drives the planet inwards. These two effects are of similar magnitude, and the net torque that determines the direction of migration depends on the local structure (Kley et al. 2012). For low-mass planets, the torque is usually negative, and the planet is quickly driven inwards. This is Type-I migration, and its rate depends on the planet's mass and the local gas density. It is driven mainly by the corotation torques (created within the corotation region, where the planet and surrounding disc material have the same average speed) and Lindblad torques (due to the spiral density waves) and the sum of the two determines the direction of migration (Kley et al. 2012).

Higher-mass planets undergo Type-II migration. Due to their stronger gravitational influence, the transfer of angular momentum to the disc becomes more efficient. The deposition of angular momentum in the disc through shock waves or viscous dissipation causes the material around the planet to recede, leading to the formation of a gap. The size of this gap will depend on the viscosity and pressure of the disc, as well as the mass of the planet (Kley et al. 2012). As a result, the gas density near the planet will be reduced, and the planet's migration will occur on a longer timescale (Ida, Tanaka, et al. 2018).

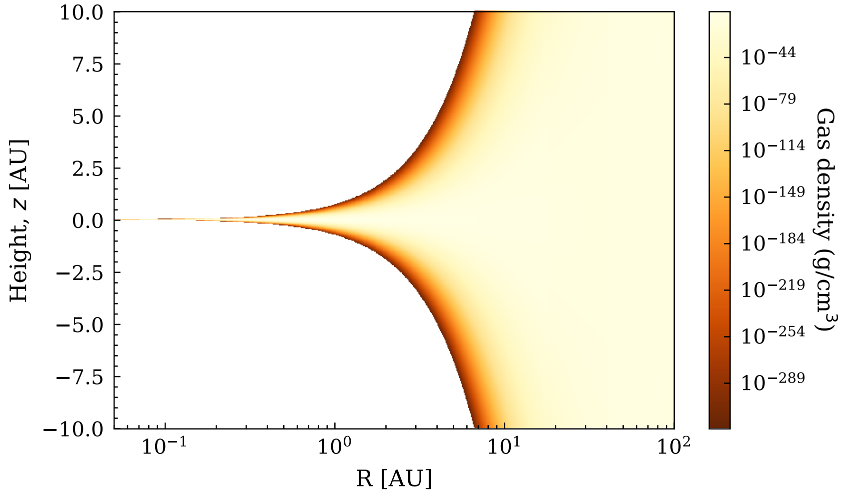

Figure 2.3: Gas density as a function of R and z. The colorbar, indicating the gas density, is a logarithmic scale and shows the steep dependence on z.

2.2 Orbital mechanics

2.2.1 The two- and three-body problems

As two massive bodies orbit each other, one can compute the gravitational interactions between them and predict their motion. Assuming the two bodies are only interacting under the force of gravity, they will orbit their mutual centre of mass (the barycentre) in an elliptical pattern. This force depends only on the relative distance between the two bodies, and is given by Newton's law of gravitation

$$F_G = G\frac{m_1 m_2}{r^2}, \tag{2.7}$$

where $G = 6.67 \times 10^{-11}\,\mathrm{Nm^2/kg}$ is the gravitational constant, m_1, m_2 are the masses of the two bodies, and r is the distance between their centres, assuming spherical bodies.

However, when adding a third body to the system, the differential equations that describe the movements of three gravitational bodies can, in general, no longer be solved analytically (Poincaré 1890). The orbits of the three bodies are chaotic, and one must use numerical methods to predict their motions. One subcase of the three-body problem is the restricted three-body problem (Szebehely 1967), where the third body has a negligible mass in comparison to the two other bodies. Assuming it is massless, it would not exert a force, and the problem would be reduced to computing the force exerted on it by the other bodies in the system. This is an accurate approximation when considering the Earth, Moon, and Sun system, for example.

Within the context of the N-body problem, it is useful to consider the region where a planet's gravity dominates over that of its host star. This is called the Hill sphere and is defined by the Hill radius, R_H, approximated for a circular orbit as

$$R_H \approx a\sqrt[3]{\frac{m}{3(M+m)}}, \tag{2.8}$$

where m is the mass of the less massive object, and M is the mass of the more massive object.

Material entering the Hill sphere of a planet can become gravitationally captured, leading to the formation of moons or planetary accretion. This material will first settle into an orbit around the planet, forming a circumplanetary disc (CPD). As the material loses angular momentum due to turbulence and viscosity, it will begin to accrete onto the planet, depleting the CPD after a few million years (Lubow et al. 2012).

2.2.2 Kepler's orbital parameters

The orbits of objects following a Keplerian motion can be described by a set of six orbital parameters. These are: semimajor axis, a, eccentricity, e, inclination i, longitude of the ascending node, Ω, argument of periapsis, ω, and a phase element, which can be t_0, the time of periapsis passage, or f, the true anomaly.

For an elliptical orbit, the semimajor axis a is defined as half the distance between the periapsis (the closest point in the orbit from the main body) and the apoapsis (the furthest point from the main body), as shown in figure 2.4. For a circular orbit, it is equal to the radius of the orbit. One can infer the period T of an object on a Keplerian orbit from the semimajor axis, and vice versa. This can be done using Kepler's third law, which states that the square of the period is proportional to the cube of the semimajor axis

$$T = 2\pi\sqrt{\frac{a^3}{GM}}, \tag{2.9}$$

where G is the gravitational constant and M is the mass of the central body of the system.

The eccentricity e describes how much the orbit deviates from a perfect circle ($e = 0$). Elliptical orbits will have $0 < e < 1$. An object with $e > 1$ would be on a hyperbolic orbit and would be considered unbound. An eccentricity $e = 1$ is a parabolic orbit.

The inclination i of an orbit is the angle between its orbital plane and the plane of reference, i.e., Earth's equatorial plane. Orbits with inclinations up to 90° are called prograde orbits (they rotate clockwise when viewed from the north pole), and those with inclinations between 90 and 180° are retrograde orbits.

The longitude of the ascending node Ω is defined for inclined orbits and is the angle measured in the reference plane spanning from the reference direction to the ascending node ☊. The nodes are the two points of intersection between the reference plane and the inclined orbit. The ascending node is the one through which the object orbits from below the reference plane to above it.

The argument of periapsis ω is also measured relative to the ascending node, but in the plane of the orbit instead. This angle spans from the ascending node to the periapsis.

The true anomaly f describes where the object is in its orbit. It is the angle formed between the periapsis and the location of the body along the direction of the orbit.

2.2.3 Mean motion resonance

Mean motion resonance (MMR) occurs when two bodies meet at the same position at every orbit of the outermost body. In other words, the orbital periods of two bodies satisfy

$$\frac{P_1}{P_2} \approx \frac{p+q}{p},$$

where P is the period of each object, p and q are integers, and q is the order of the resonance. For example, a 2:1 resonance is first order and a 5:3 resonance is third order. The higher the order of the resonance, the stronger it impacts the dynamics of the system.

Planets may also be in mean motion resonance, even if their period ratios are not exact. One can define the resonant angle librating over a value, $\theta_{c:b}$, between two planets b and c, as (in the case of PDS 70 Bae et al. 2019; Wang et al. 2021)

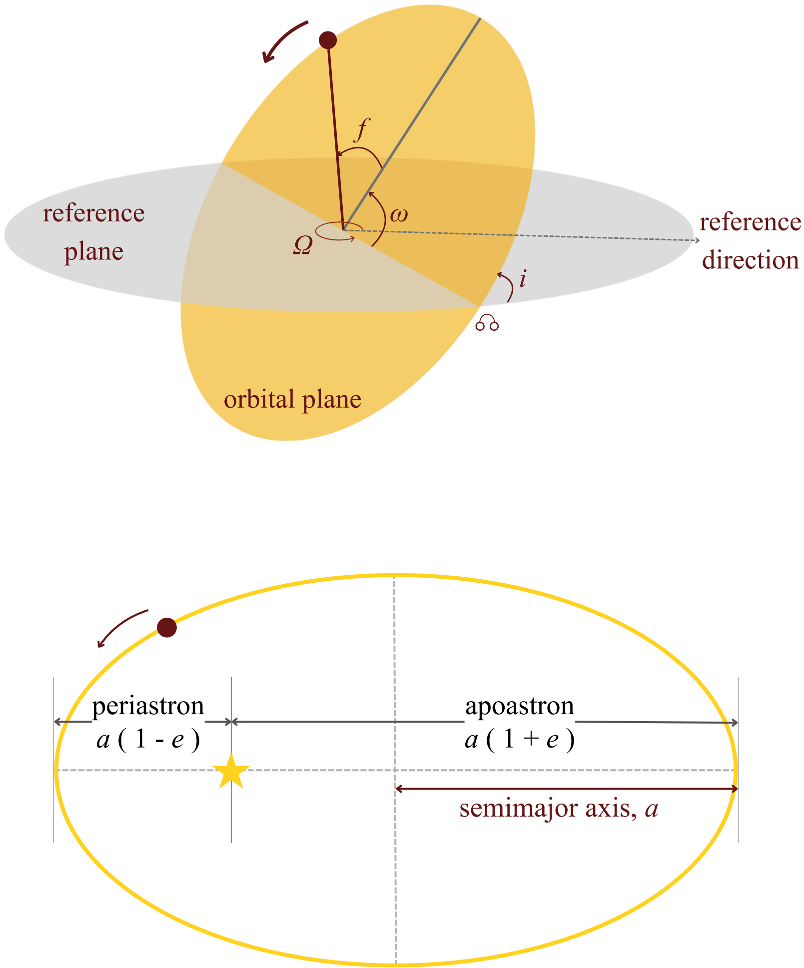

Figure 2.4: Schematics representing Kepler's orbital parameters.

$$\theta_{c:b} = \lambda_b - 2\lambda_c + \varpi_b, \tag{2.10}$$

where $\varpi = \Omega + \omega$ is the longitude of periastron and $\lambda = \varpi + M$ is the mean longitude, with M as the mean anomaly. Whereas the true anomaly is the angle swept out by an elliptical orbit from periastron to the location of the object, the mean anomaly is the angle swept out by a circular orbit with the same period as the elliptical. The opposite resonance angle $\theta_{b:c}$ can also be defined using the values relative to the outer planet's argument of periastron. An object in resonance should have a resonant angle that librates around zero over time.

Resonances can work to either stabilise a system or destabilise it. One example is the Cassini Division in Saturn's rings. This region is depleted of small bodies since they would be in resonance with Mimas, one of Saturn's moons. The moon gravitationally perturbs the objects in this dense region, causing them to collide and grind down, eventually forming a gap. This only occurs for objects in elliptical orbits, since it is the velocity differences at peri and apoastron that can cause collisions.

The PDS 70 planets are likely in a 2:1 resonance (e.g. Bae et al. 2019; Toci et al. 2020; Do Ó et al. 2025) and may have migrated early on into these resonances, before they carved a gap in the gas disc (Toci et al. 2020).

2.3 The physics of planetesimals

Planetesimals are kilometre-sized solid bodies formed within protoplanetary discs and constitute the fundamental building blocks of planetary formation (Johansen, Blum, et al. 2014). They originate from small dust grains embedded in the gaseous disc, which stick together upon collision to form larger aggregates, called pebbles. These pebbles can become concentrated into dense clumps via streaming instabilities (Youdin et al. 2005), a process in which interactions between solid particles and the surrounding gas lead to local material concentrations. Once a sufficiently high local mass density is achieved, these overdense clumps collapse into kilometre-sized planetesimals (Johansen, Oishi, et al. 2007).

2.3.1 Gas drag

Similar to planets, smaller bodies will also interact with the disc they are embedded in, and other forces may be necessary to include when computing their orbits. Namely, in regions where gas density is high, planetesimals moving at high speeds may feel the influence of gas drag. Planets, on the other hand, have large enough masses that the effect of gas drag is negligible. To compute the deceleration felt by planetesimals embedded in a gaseous disc, one needs the relative velocity between the gas (moving at approximately Keplerian speed) and the planetesimals, as well as the stopping time.

The stopping time is the characteristic timescale over which this relative velocity becomes damped. It can be calculated as was done in Perets et al. 2011; Guillot et al. 2014; Eriksson et al. 2021, given in equation 2.11

$$t_s = \left(\frac{\rho}{\rho_\bullet} \frac{v_{\rm th}}{R_{\rm pl}} \min\left[1, \frac{3}{8}\frac{v_{\rm rel}}{v_{\rm th}} C_D(Re)\right] \right)^{-1}, \tag{2.11}$$

where $\rho_\bullet$ is the solid density of the planetesimals, $R_{\rm pl}$ is their radius, and $v_{\rm th} = \sqrt{8/\pi}c_s$ is the gas thermal velocity. The planetesimals are assumed to be icy, which yields a solid density of $1000\,{\rm kg/m^3}$. Three different radius values will be tested in this work: 1, 10, and 100 km. In the second term of the min function in equation 2.11, $v_{\rm rel}$ is the relative velocity between the planetesimals and the gas, C_D is the dimensionless drag coefficient, and Re is the Reynolds number. The dimensionless drag coefficient is defined as a function of the Reynolds number, which can be found by fitting empirical data (Perets et al. 2011)

$$C_D = \frac{24}{Re}(1 + 0.27Re)^{0.43} + 0.47(1 - \exp[-0.04Re^{0.38}]). \tag{2.12}$$

The Reynolds number, Re, quantifies the importance of viscous forces vs inertial forces in a fluid and is given by (Guillot et al. 2014)

$$Re = \frac{4R_{\rm pl}v_{\rm rel}}{c_s l_g}, \tag{2.13}$$

where $l_g \sim 5 \times 10^{-6}{\rm kg\,m^{-2}}/\rho$ is the mean free path of the gas (Supulver et al. 2000).

From figure 2.5, it can be seen that the stopping time increases substantially with the distance to the star, R. In the gap and outer disc, the stopping time is several orders of magnitude larger than the total age of the system ($5{\times}10^6$ yr). Therefore, gas drag can be considered negligible in these regions. However, within the inner disc, the stopping time starts becoming comparable, or even much smaller, than the system's age, and the effect of gas drag may not be ignored. This is especially true for smaller planetesimal sizes.

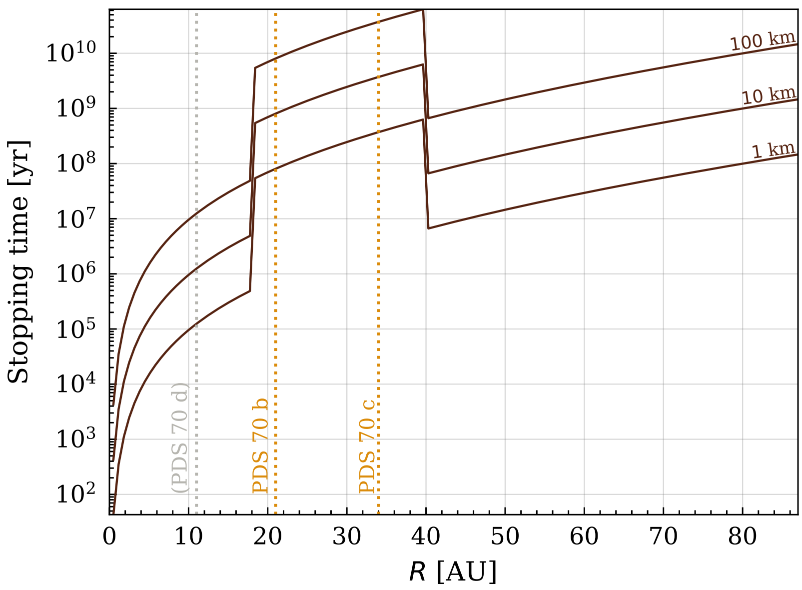

Figure 2.5: Stopping time for different planetesimal radii as a function of distance to the star for particles distributed from 0 to 87 AU. The semimajor axes of the planets are plotted at (11), 21 and 34 AU.

Finally, the deceleration due to the gas drag force, $\mathbf{a}_{\text{drag}}$, can be calculated as the ratio between the relative velocity between the gas and the planetesimals ($\mathbf{v}_{\text{rel}} = \mathbf{v}_{\text{pl}} - \mathbf{v}_{\text{gas}}$), and the stopping time

$$\mathbf{a}_{\text{drag}} = -\frac{1}{t_s}\mathbf{v}_{\text{rel}}. \tag{2.14}$$

2.3.2 Ablation

As a planetesimal moves through a hot gaseous medium, such as the protoplanetary disc near the star, it will experience friction heating and irradiation. The heating of this object's surface can cause its material to vaporise, or become stripped away, leading to mass loss over time. This process is called ablation. I estimate the mass loss due to ablation to determine whether it affects the lifetime of planetesimals and if it could represent a means of water delivery in the inner disc. To determine the mass loss due to ablation from the surface of an object, one must first determine the equilibrium surface temperature of a planetesimal, T_{pl}. I follow the process described in Ronnet et al. 2020 and seen in equation 2.15. The first two terms in the equation are heating terms, one due to radiation from the disc and another due to gas friction. The third term corresponds to the cooling due to the ablation of volatile ices. The calculated temperature is such that these terms are assumed to be in equilibrium

$$T_{\text{pl}}^4 = T_{\text{d}}^4 + \frac{C_D \rho_{\text{gas}} v_{\text{rel}}^3}{32\sigma_{\text{SB}}} - \frac{P_{\text{sat}}(T_{\text{pl}})}{\sigma_{\text{SB}}}\sqrt{\frac{\mu_{\text{H}_2\text{O}}}{8\pi R_{\text{g}} T_{\text{pl}}}} L_{\text{H}_2\text{O}}. \tag{2.15}$$

Here, T_{d} is the local temperature of the disc (see equation 2.5), C_D, ρ_{gas}, and v_{rel} are as defined in the previous section, σ_{SB} is the Stefan-Boltzmann constant, $P_{\text{sat}}(T_{\text{pl}})$ is the saturated vapour pressure of water, $\mu_{\text{H}_2\text{O}}$ is the molecular weight of water, R_{g} is the ideal gas constant, and $L_{\text{H}_2\text{O}}$ is the latent heat of vaporization of water. The values for these constants are expressed in table 2.1.

The saturated vapour pressure is the pressure exerted by a vapour when it is in equilibrium with its liquid phase at a given temperature and has a strong temperature dependence. It is given by the following equation, assuming the vapour is water (Wagner et al. 1993)

Table 2.1: Table of constants used in determining the surface temperature of a planetesimal (equation 2.15).

Constant	Value	Constant	Value
σ_{SB}	$5.670\,37 \times 10^{-8}\,\mathrm{W\,m^{-2}\,K^{-4}}$	R_g	$8.314\,\mathrm{J\,mol^{-1}\,K^{-1}}$
μ_{H_2O}	$18\,\mathrm{g\,mol^{-1}}$	L_{H_2O}	$3 \times 10^{6}\,\mathrm{J\,kg^{-1}}$

$$\ln \frac{P_{sat}(T_{pl})}{P_c} = \frac{T_c}{T}\left(a_1\tau + a_2\tau^{1.5} + a_3\tau^3 + a_4\tau^{4.5} + a_5\tau^4 + a_6\tau^{7.5}\right), \quad \text{where} \tag{2.16}$$

$$\tau = 1 - \frac{T}{T_c}.$$

T_c and P_c are the temperature and pressure of water at the critical point, and the coefficients a_n, where $n = 1, 2, ..., 6$, are empirically determined. All constants are given in table 2.2. A plot of the dependency of the saturated vapour pressure of water is shown in figure A1.

Table 2.2: Constants used in the equation for saturated vapour pressure of water (equation 2.16).

$T_c = 647.096\,\mathrm{K}$	$P_c = 22.064\,\mathrm{MPa}$	
$a_1 = -7.85951783$	$a_2 = 1.84408259$	$a_3 = -11.7866497$
$a_4 = 22.6807411$	$a_5 = -15.9618719$	$a_6 = 1.80122502$

One can then use this planetesimal temperature to determine the mass ablation rate from the surface of the object as

$$\dot{m}_{abl} = -4\pi R_{pl}^2 P_{sat}(T_{pl})\sqrt{\frac{\mu_{H_2O}}{2\pi R_g T_{pl}}}. \tag{2.17}$$

Chapter 3

Methods

For this thesis, several simulations were performed with different choices of setup parameters, explained and justified in the sections below. The entirety of the code written for performing and analysing these simulations was written in Python (with the exception of the custom REBOUNDX gas drag force, which was written in C). Before that, I would like to introduce N-body simulations in general and how the REBOUND code can be used for this purpose.

3.1 N-body simulations and Rebound

Solving the differential equations that define the motion of two bodies (the two-body problem) is straightforward. However, once a third body is added, this task generally becomes analytically impossible, and one must resort to numerical approximations. REBOUND (Rein and Liu 2012) is an N-body code that contains several integrators, suited for different purposes, to calculate the future positions of bodies interacting gravitationally. The integrator used for simulations in this project is REBOUND's default `IAS15` (Rein and Spiegel 2015). This is a 15th-order non-symplectic integrator, designed to reach machine precision (10^{-16}). It stands out for its accuracy and its ability to handle non-conservative forces (it does not require the system to be Hamiltonian, as a classic symplectic integrator). It also uses an adaptive timestep, meaning the time between consecutive calculations, $\mathrm{d}t$, varies with the frequency and complexity of interactions between objects in the simulation. For example, if one is simulating a stable system of two planets orbiting a star at large separations, the timestep $\mathrm{d}t$ will be larger, and the simulation will progress relatively quickly while still maintaining accuracy. If, on the other hand, one is dealing with a collision between bodies in which the system dynamics change rapidly, the adaptive integrator will choose a smaller timestep to resolve these fast interactions. This integrator was chosen for this project because of its ability to handle close encounters, which can occur when massless test particles (representing planetesimals) interact with massive bodies. `IAS15` can also handle additional, non-conservative forces implemented, for example, through REBOUNDX, which was used to account for gas drag in simulations of the inner system.

3.2 Orbital parameters

All simulations in this thesis use the orbital parameters for the two/three planets given in Trevascus et al. 2025. This is the most recent paper that provides full tables of orbital parameters and considers both the two-planet and three-planet cases. It also includes configurations that are "N-body stable" after integrating for 2 Myr. The criteria chosen in this paper to define stability are that 1) the planets never reached one Hill radius separation from each other (~ 3.3 AU) and 2) no planets were ejected to > 40 AU from the PDS 70 star. It is assumed that the authors chose this second criterion because a planet entering the disc, which begins at ~ 40 AU, could disturb or even destroy it. Table 3.1 and table 3.2 are the orbital parameters used for this thesis and were taken from the mean value of the "Stable (inc. N-body)" column

Table 3.1: Orbital parameters used in the simulations with two planets. Values (including the stellar mass) are taken from the mean value of the "Stable (inc. N-body)" column in Table 3 of Trevascus et al. 2025. Note that the inclinations are relative to the disc inclination of 128.3°.

Planet	Mass [M_J]	e	a [AU]	i [°]	ω [°]	Ω [°]
PDS 70 b	1.4	0.16	20.7	2.3	190	176
PDS 70 c	6.4	0.042	33.9	1.5	77	158.0
$M_\star = 0.952\,M_\odot$						

Table 3.2: Same as table 3.1, but taken from Table 4 of Trevascus et al. 2025 and for the three-planet configuration.

Object	Mass [M_J]	e	a [AU]	i [°]	ω [°]	Ω [°]
PDS 70 d	0.4	0.25	10.7	22.7	29.0	144.0
PDS 70 b	0.7	0.131	21.1	0.4	191.4	174.3
PDS 70 c	2.4	0.033	35.3	0.2	63.0	159.8
$M_\star = 0.965\,M_\odot$						

from Table 3 and Table 4 in Trevascus et al. 2025, respectively. The orbital parameters given for each planet are: eccentricity (e), semimajor axis (a), inclination (i), argument of periastron (ω), and longitude of the ascending node (Ω). Note that the reference provides absolute inclinations, whereas here I present inclinations relative to the disc. The star is given only a mass and is by default located at $x = y = z = 0$.

To fully describe an orbit, there is one more parameter that must be defined, and that is the true anomaly, f. This represents the phase between the objects, or the angle between the orbit's periapsis and the point of the orbit where the body is initialised. It is taken from a random normal distribution from 0 to 2π radians. Further justification for this is given in section 3.3.

In all simulations, the integration is performed in a loop, where orbital parameters are evaluated every 0.2 years. This also automatically sets the maximum timestep allowed.

3.3 Stability testing

The values presented in table 3.1 and table 3.2 were published a couple of months after the start of this thesis. Therefore, I had initially set up my simulations to use the mean values of the "Dynamically Stable" column of Table 3 in Wang et al. 2021, which included higher masses for the two planets (3.24 and 7.5 M_{Jup} respectively). During these simulations, I realised the chaotic nature of the system, and that initialising it with the same orbital parameters but changing the phase (in this case, controlled in REBOUND via the true anomaly parameter, f) could lead to drastically different outcomes (see figure 3.1). The main parameter that affected the system's stability was the masses of the two planets, which were also poorly constrained.

This motivated the exploration of the mass uncertainty range to try to find a combination of masses that would lead to a more likely survival of the system. For a certain mass combination, the more stable a configuration is, the smaller the effect the choice of initial phase should have. Although it is not known if the PDS 70 system will remain stable or even if it is currently stable, we do know that the planets exist in the configuration known today. Therefore, it is assumed that the planets are stable on (at least) a 1 Myr timescale, from which conclusions throughout the thesis involving such timescales are based. Highly chaotic systems are disfavoured because of the increased chance of planets being ejected from the system.

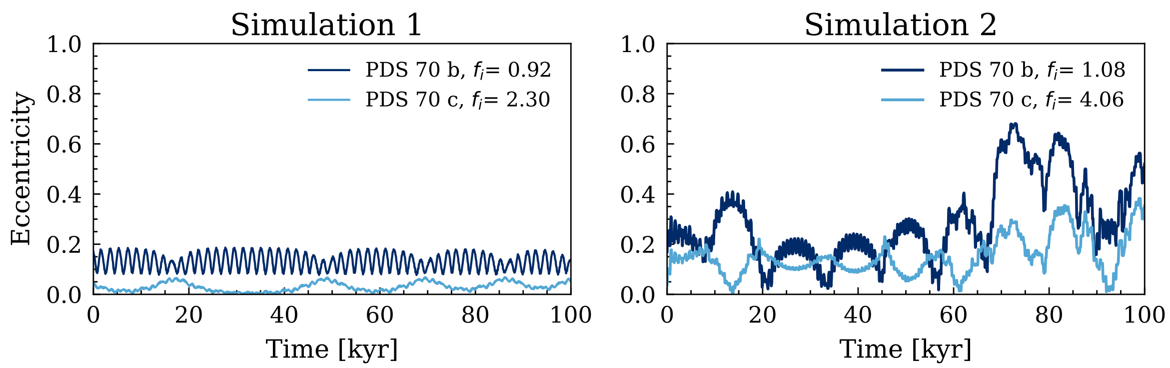

Figure 3.1: Example of the eccentricity evolution of two planets in two distinct simulations with parameters set to the mean values of the "Dynamically Stable" column of Table 3 in Wang et al. 2021. The two simulations vary only in the chosen initial value for true anomaly, which was drawn randomly from a distribution from 0 to 2π in each case and indicated in the legend.

For each mass combination, 100 simulations were performed. The initial parameters in each are identical except for the true anomaly, which is randomised every time. Then, simulations are judged based on pre-defined stability criteria. After 2 Myr, a simulation is deemed stable if:

1. No planet has an eccentricity above 1;
2. No planets cross orbits at any time, that is, $a_b(1 + e_b) < a_c(1 - e_c)$ and, in the case of the third planet, $a_d(1 + e_d) < a_b(1 - e_b)$;
3. No planet may cross the outer edge of the disc, i.e., 87 AU.

The last criterion is a more loose version of what was chosen in Trevascus et al. 2025 and is based on the disturbance the disc would feel if a planet were to cross it and potentially accrete material. Below, I describe the range of masses sampled in both the two- and three-planet cases.

3.3.1 The two-planet case

As stated previously, the simulation is initially set up with the orbital parameters given in Wang et al. 2021 (and later table 3.1), except for the masses, which I let vary between 1 and 12 M_{Jup} for both planets (in steps of two, i.e., 1, 3, 5, 7, 9, 11), leading to a total of 36 combinations. The final simulation is integrated forward 2 Myr to remain consistent with Trevascus et al. 2025. This was the chosen integration time as it is the lower bound for the type II migration timescale of this system (section 2.1.3), that is, the characteristic time over which a planet will change its orbit due to interactions with the disc.

3.3.2 The three-planet case

After Trevascus et al. 2025 was published, I decided to do a stability search with the three-planet configuration. This was done for completion and to test specific combinations (a range of stable masses is given in the referenced paper, but it is unclear which combinations of masses within the uncertainty ranges yield stable outcomes). For these tests, I chose smaller mass ranges due to the narrower uncertainty windows provided in this new paper and based on the results of the two-planet simulations. PDS 70 b was allowed to range from 1 to 3 $\mathrm{M_{Jup}}$ in increments of 0.5; PDS 70 c was more unconstrained, and ranged from 1 to 7 $\mathrm{M_{Jup}}$ in steps of 2; and PDS 70 d ranged from 0.5 to 2 M_{Jup}, again in steps of 0.5. This resulted in a total of 80 mass combinations being tested.

3.4 Simulating particles in a disc

The main simulations of this thesis will include thousands of test particles in a disc, representing planetesimals. These particles are defined to be massless since their masses are several orders of magnitude smaller than the main bodies in the system (star and planets) and can be neglected. This means that they feel the gravity from the planets and the star, but do not exert any gravitational force themselves. This is done to drastically improve computational time. The disc simulations are split into two, depending on where particles are initialised. The outer disc simulations include particles initialised with semimajor axes from 54 to 87 AU and do not include a gas drag force, since the gas density of these regions is not strong enough to have an effect on the orbits of particles. The inner disc simulations are a continuation of the outer disc simulations for the particles that end up reaching a distance $R < 18$ AU. These do include a gas drag force since in these regions, the density is high enough that gas drag might be important in the determination of particles' orbits. The two simulation types are described in more detail in section 3.4.2 and section 3.4.3, respectively.

3.4.1 Particle classification

The bulk of this thesis will be dedicated to analysing the orbits of massless test particles, representing planetesimals, in a PDS 70-like system. Depending on a particle's orbital parameters at each timestep, it can be categorised in one of the following ways: ejected, captured, collided, migrated (applicable in the outer disc simulations), star-grazing (applicable in the inner-disc simulations), or survived.

A particle is considered ejected when its eccentricity is greater than or equal to one ($e \geq 1$), while simultaneously having a position, $R = \sqrt{x^2 + y^2 + z^2}$, larger than 200 AU, measured in the centre of mass reference frame. This second requirement ensures that ejected particles are sufficiently far from the system so they cannot become bound again. When detected, these particles are deleted.

A captured particle has entered the Hill sphere of the planets and remained there for several orbital timescales. This requirement is necessary to avoid classifying temporary flybys, which are common (Carusi et al. 1979), as true captures. Based on integrations of the orbits of fragments around Jupiter, Benner et al. 1995 found that the median capture duration is short-lived around 8 Jupiter orbits, that is, close to 100 years. However, the distribution of capture times reaches several hundred years. The relevant timescale for long-term captures increases with orbital distance. Particles orbiting the PDS 70 planets at the edge of their Hill sphere (at approximately 1 Hill radius) would have very long periods, comparable to the orbital period of the planet, which are roughly 100 and 200 years (see equation 2.9). In this regime, the dynamical evolution is slow and temporary captures can remain bound for many orbits before escaping. For this reason, captures are only defined as such if a particle remains within the planet's Hill sphere for 10000 years or more. This corresponds to roughly 50 PDS 70 c orbits. After this time, the particle's parameters, along with the hash (particle ID) of the planet responsible for the capture, are saved, and the particle is removed from the simulation. This is done because 1) the particle is no longer interesting for our purpose of making and tracking exocomets, and 2) to avoid wasting computing time, since the timestep chosen by the adaptive integrator will be small and will slow down the simulation.

A particle that collides with a planet (particle-particle collisions are assumed to be negligible) is also removed from the simulation. `REBOUND` includes a collision detection module which checks when the distance between two particles is smaller than the sum of their radii. The "line" method is used to search for collisions, which checks for overlapping particles during a timestep, by assuming a linear travel between the start and finish of that timestep. Since the integrator is adaptive, a shorter timestep is chosen when two bodies are in close vicinity with one another, increasing the validity of the linear trajectory approximation. For the outer disc simulations, a particle radius of 100 km and a planet radius of 10 R_{Jup} for all planets are chosen. The actual planetary radii are likely much smaller than this; however, it is assumed the planets are surrounded by circumplanetary discs, inside which, up to about 10 R_{Jup} from the planet's centre, the temperature is high enough such that a particle crossing it would ablate (Ronnet et al. 2020). Although the choice of radius may be an overestimate, it will lead to a more conservative count of the number of exocomets. The inner disc simulations are done for three different particle radii (1, 10, and 100 km).

In the outer disc simulations, if any of the planetesimals reaches a distance from the star of less than 18 AU ($R < 18$ AU), it is considered a “migrated” particle and its parameters, as well as the time of migration, are saved.

A star-grazing particle reaches a periastron distance of 0.4 AU or less while having a position $R < 5$ AU. This guarantees it will not encounter a planet on its way inwards, and the calculated periastron distance will remain constant. The value of 0.4 AU is somewhat arbitrary but has been chosen to be consistent with star-grazing particles in N-body simulations of the Beta Pictoris system (Jaworska et al. 2026). In the case of PDS 70 , to reproduce the exocomet radial velocities found in Novais et al. 2025, exocomets could have periastron distances anywhere from 0.1 to 4 AU, with which the choice of 0.4 AU is consistent.

All other particles are classified as “survived”.

3.4.2 The outer disc

The purpose of this set of simulations is to understand whether planetesimals in the outer disc can get scattered past the carved gap and into the inner disc. This is a simple initial check for the feasibility of the eventual creation of exocomets.

To simulate a PDS 70-like system with an outer disc of planetesimals, the planets were given the same parameters as shown in table 3.1 and table 3.2 for the two and three-planet cases, respectively, once again randomising the true anomaly. The star was given the mass indicated in the same tables. Then, 50,000 test particles were added to the outer region of the system, with a random distribution of semimajor axes from 54 to 87 AU and inclinations from -10 to $10°$. Their eccentricities were set to zero, as it can be assumed that they have circularised from their time embedded in a disc. To increase efficiency, the code was parallelised such that particles could be split over 50 computer cores, each one dealing with a slightly different configuration of planets (due to the phase randomisation) and 1000 particles. As was seen in the previous section, unstable configurations can arise, and the same stability criteria as before were adopted for these simulations. When a system is deemed unstable, that particular simulation is stopped and restarted with a different randomisation of true anomalies. In this case, the integration time is set to 5 Myr, the approximate age of the system, and orbital parameters are evaluated every 0.2 years. If a particle is flagged as migrated, its parameters are saved. If such migrated particles exist, this would be a supporting argument for exocomets.

3.4.3 The inner disc

As shown in section 2.1, gas drag has little effect in the outer disc since the stopping time is many orders of magnitude larger than the simulation time. However, entering the inner regions of the system, the stopping time decreases significantly with proximity to the star, and gas drag may have an effect on the orbits of close-in particles. To implement the effect of gas drag, I use the `REBOUNDx` extension (Tamayo et al. 2020) to include additional forces in a `REBOUND` simulation. To do this, I created a custom force that adds the acceleration calculated using equation 2.14 to the particles' computed acceleration at each timestep. This is done in a separate file, written in C, which is called at the beginning of the simulation.

The inner disc simulations are constructed to be a continuation of the outer disc ones, considering only the particles that reach the inner disc and “turning on” a gas drag force. To guarantee a seamless transition, each migrated particle is placed in the new simulation with the exact parameters it had when flagged as $R < 18$ AU. This assures they have spent negligible time in the inner disc. The choice of 18 AU is also a conservative one, since here, the stopping time is jag älskar vintergatan one to three orders of magnitude higher than the simulation time (depending on the planetesimal radius - see figure 2.5). To perfectly reproduce the previous conditions, the positions of the massive bodies were also saved and reused in the new simulation. In this case, parallelisation is not possible - each simulation includes only

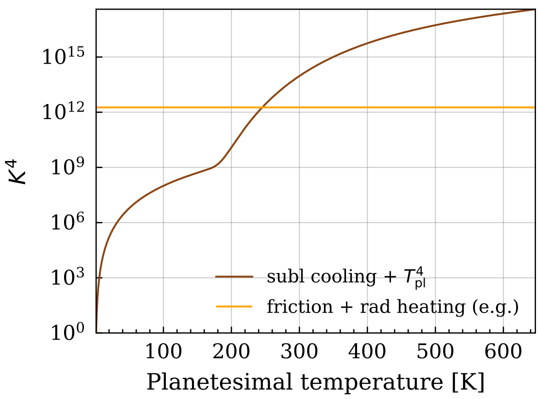

Figure 3.2: Example of the intersection between the $T_{\rm pl}$ dependent and independent terms given in equation 3.1. This is an example of the temperature determination of a particle with a semimajor axis of 2 AU and an eccentricity of 0.8, a plausible combination for an exocomet candidate.

one test particle, and the number of simulations performed equals the number of migrated particles. These simulations are performed for a shorter time of 1 million years since I do not simulate the evolution of gas, and must assume it remains constant over the simulated time. These simulations are repeated three times, for the three different planetesimal radii being tested (1, 10, and 100 km). Once again, some configurations turn out to be unstable. These cannot be rerun because the initial conditions are fixed, so they are simply excluded from the final results. This leads to the total number of particles being lower than 50,000 in the three-planet simulations, where these instabilities arose.

To determine the mass loss of a planetesimal due to ablation, I use the orbital parameters of star-grazing particles from the moment they are classified as such and determine the velocity vector at every point of that orbit using the tool `jaxoplanet` (Soichiro Hattori et al. 2024). With this, as well as the position of the particle throughout its orbit, I compute its temperature from equation 2.15. Since the cooling term in equation 2.15 depends on the planetesimal temperature itself, the equation is solved by finding the intersection between the $T_{\rm pl}$-independent terms and the $T_{\rm pl}$-dependent terms. That is, I find where

$$T_{\rm pl}^4 + \frac{P_{\rm sat}(T_{\rm pl})}{\sigma_{\rm SB}}\sqrt{\frac{\mu_{\rm H_2O}}{8\pi R_{\rm g} T_{\rm pl}}}L_{\rm H_2O} = T_{\rm d}^4 + \frac{C_D \rho_{\rm gas} v_{\rm rel}^3}{32\sigma_{\rm SB}}. \tag{3.1}$$

The ablation rate is then calculated at every point in the particle's orbit and integrated to find the total ablation per orbit

$$\Delta M_{\rm abl} = \dot{M}\, dt,$$

where dt is the particle's period divided by 10000. This assumes that changes in orbits occur on timescales longer than the time it takes a particle to fully ablate. The instantaneous ablation rate calculated from equation 2.17 for a particle located within the disc at periastron distance is given in figure 3.3 for the three planetesimal sizes. The figure shows what the predicted ablation rates are for particles with eccentricities and periastron distances typical of star-grazers and can be used as a "reality check". In practice, the results given in section 4.3.1 will show several added layers of complexity since the ablation will be calculated throughout the entirety of an orbit and not at one single point. Additionally, dependencies on varying orbital parameters, such as eccentricity and inclination, must be untangled.

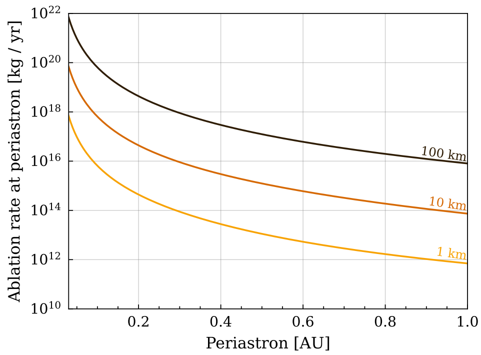

Figure 3.3: Ablation rates of particles calculated at periastron from equation 2.17. Particles have eccentricities of 0.9 and varying semimajor axes from 0.3 to 10 AU. Particles are assumed to be located in the disc ($i = 0°$). The rates are shown for the three planetesimal radii tested in this thesis (1, 10, and 100 km).

CHAPTER 4

RESULTS & DISCUSSION

4.1 STABILITY TESTING

The results of the stability tests with several mass combinations are presented in figure 4.1 for the two- and three-planet cases.

Considering the two-planet case shown in figure 4.1a first, where both planets can range from 1 to $11 M_{\text{Jup}}$, there are clear regions of stability and instability. One immediate conclusion can be drawn by looking at the bottom right corner, where the inner planet PDS 70 b is (much) more massive than the outer planet, PDS 70 c. These cases are highly unstable, especially when PDS 70 b is four or more Jupiter masses more massive than PDS 70 c. However, the opposite cannot be said - when PDS 70 b is the less massive companion, the system generally remains stable, regardless of the mass difference between the two planets. For this reason, from a stability point of view, constraining the mass of PDS 70 c remains challenging.

Given the presence of a circumplanetary disc that could supply the outer planet with material (Benisty et al. 2021), it would be reasonable to expect the outer planet to be more massive. As discussed in section 1.4, the inner planet's smaller semimajor axis results in a smaller Hill radius, so less material becomes trapped in the CPD. This, together with the possibility of the outer planet trapping material, could lead to the inner planet growing less.

The results of these simulations generally agree with literature where the masses of the planets are modelled and compared to observations. Stolker et al. 2020 discusses evolutionary models that use PDS 70 b's luminosity to place constraints on its mass. Assuming the planet has an accretion rate of $5{\times}10^{-7}\ \mathrm{M_{Jup}/yr}$, determined as the lower limit by Hashimoto, Aoyama, et al. 2020 (see section 1.3.2), this places an upper limit on the mass of the planet at approximately $1.5 M_{\text{Jup}}$. From the simulations presented in this thesis, an inner planet with such a mass would likely be stable with a second planet of any of the tested masses, up to $11 M_{\text{Jup}}$. On the other hand, Portilla-Revelo et al. 2023 combines analysis of the gas depletion within the gas with hydrodynamical models performed by Duffell et al. 2015 to estimate a mass value of about $4 M_{\text{Jup}}$ for each planet. Although this is higher than the mass determined by Stolker et al. 2020 for the inner planet, it is still a likely stable configuration based on figure 4.1a.

In summary, a configuration in which the innermost planet is the least massive appears to provide a greater probability of stability. In particular, if planet b has a mass of 5 Jupiter masses or more, it becomes highly unlikely that planet c would be less massive by more than 4 jupiter masses. Constraining the mass of PDS 70 c in any other case cannot be done dynamically, as low PDS 70 b masses (especially below 3 M_{Jup}) are stable with practically any outer planet mass. In general, lower masses are favoured from a stability probability point of view over higher masses, particularly for PDS 70 b.

Moving on to the three-planet case shown in figure 4.1b, it is clear that the addition of the third planet can greatly disturb the system. The increased instability comes from the transition from the two bodies orbiting the star to three bodies, as discussed in section 2.2.1. The number of solutions for the 3-body

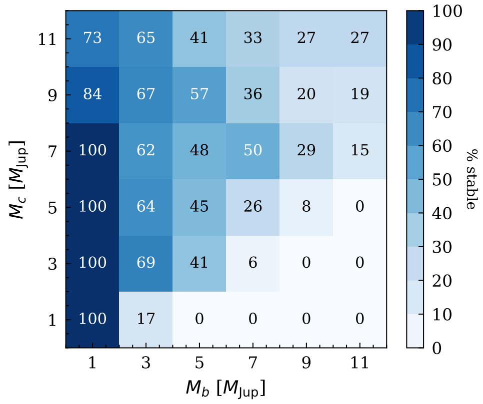

(a) Probability of stability in the two-planet case.

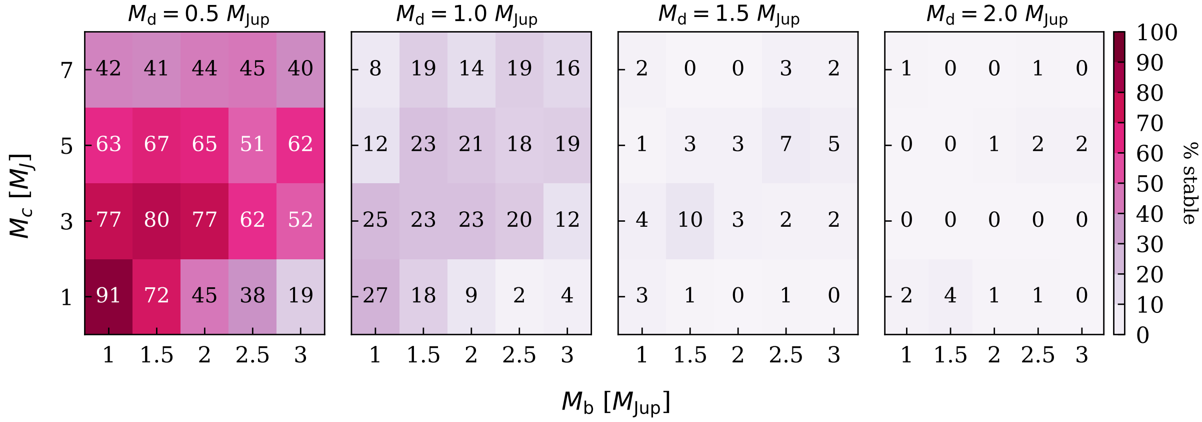

(b) Probability of stability in the three-planet case.

Figure 4.1: Percentage of stable simulations in the case of two and three planets. In both figures, the colorbar ranges from 0 to 100 and refers to the percentage of simulations that "survived" after an integration of 2 Myr, according to the stability criteria described in section 3.3. Since 100 simulations were performed for each mass combination, this percentage directly corresponds to the number of simulations retained. The figures show that lower masses are often more stable and that the inclusion of a third planet has a large disturbance on the overall stability of the system.

problem is infinite, and the number of gravitational pathways becomes more complex and unpredictable. Small perturbations grow over time, and instabilities become much more likely. In fact, none of the tested configurations gives a 100% stable solution, and the most likely configuration is one of low masses - 0.5, 1, and $1 M_{\rm Jup}$ from the inner to the outer planet. The same trend as before is followed, where a massive inner planet ($M_d \geq 1.0 M_{\rm Jup}$) causes large instabilities.

These simulations were also done by forcing the planets to have semimajor axes/periods that would put them in a 4:2:1 resonance, and the results are presented in figure A2. This made the system even more unstable, likely because it forced the planets into closer separations.

Assuming that the confirmed planets have masses of at least $1 M_{\rm Jup}$ (Wang et al. 2021), which is consistent with the minimum gap opening mass of $\sim 0.5 M_{\rm Jup}$ (Edgar et al. 2007), it is unlikely that the third planet is more massive than $1 M_{\rm Jup}$. The masses of the planets are a determining factor in the rates at which planetesimals cross the gap, as is discussed in the next section (section 4.2.1. The simulations from here onwards will use $M_c = 6.4 M_{\rm Jup}$ and $M_c = 2.4 M_{\rm Jup}$ for the two- and three-planets respectively (see table 3.1, table 3.2, and Trevascus et al. 2025). This difference, based on both literature and this work (see figure 4.1), will be important for interpreting the subsequent results in this thesis.

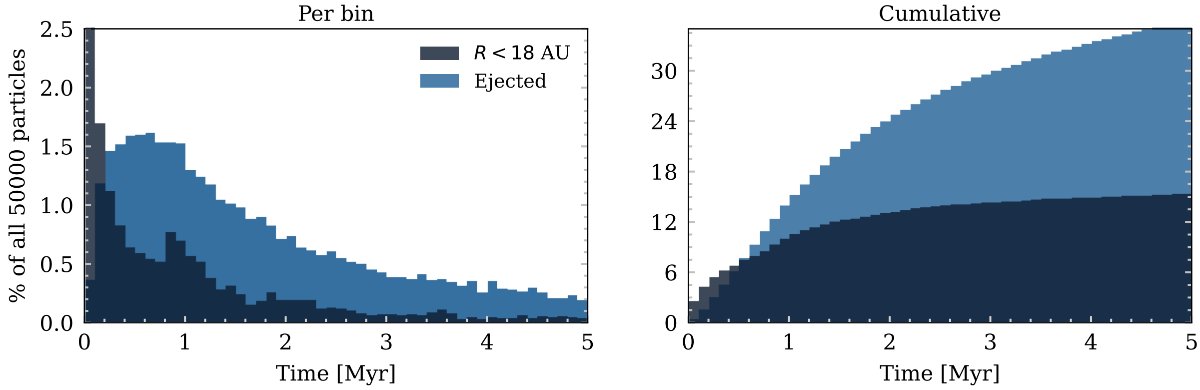

(a) Two-planet case.

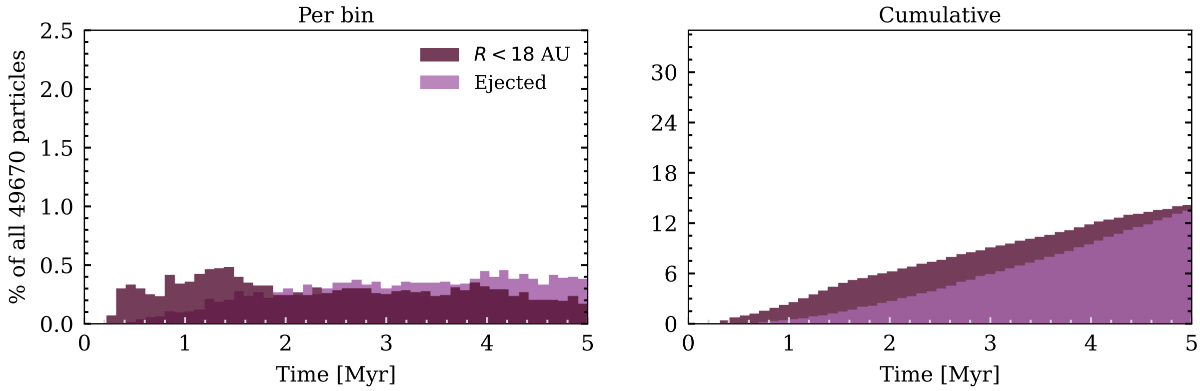

(b) Three-planet case.

Figure 4.2: The fate of particles over time. The darker colours show the number of particles that crossed into the inner disc over time, and the lighter colours show the number of ejected particles over time.

4.2 Simulating the outer disc

4.2.1 Migration rates

The next set of results attempts to answer whether planetesimals in the outer disc can cross the gap formed by the two gas giants and be scattered into the inner disc at < 18 AU. Figure 4.2 shows the results of these simulations for both planet-number cases. It can be seen that, in both cases, the planets can scatter the planetesimals inward. In the two-planet case (see figure 4.2a), this scattering is most efficient in the first million years, where the disc of planetesimals is still settling. It is also shown that the two-planet case has a much larger fraction of ejected particles. This is due to the much larger mass given to PDS 70 c (see table 3.1 VS table 3.2). In contrast, the first bin of figure 4.2b is almost empty - due to the lower masses of the planets in this simulation, it takes longer for the disc to become disturbed due to interactions with the planets. The migration and ejection rates in this case are steadier throughout the duration of the simulation. Considering the migration rates in the last 1 million years, the mean is roughly 0.45% per Myr in the two planet case and 2.4 % per Myr in the three planet case (best seen in the cumulative distributions - right panels - of figure 4.2).

The reason the calculated rates are only for the last 1 million years is that the first ~ 1 million years of simulation are more chaotic than the final millions of years. This is especially the case for the two-planet case, as seen in figure 4.2, where most planetesimal scattering occurs within the first 1 million years. For this reason, it would be interesting to test whether the results are largely influenced by the initial chaos, which is a direct consequence of the simulation setup and may not accurately reflect the system as it is today. Figure 4.3 is a collection of branching ratio plots, which show the distribution of particle fates as

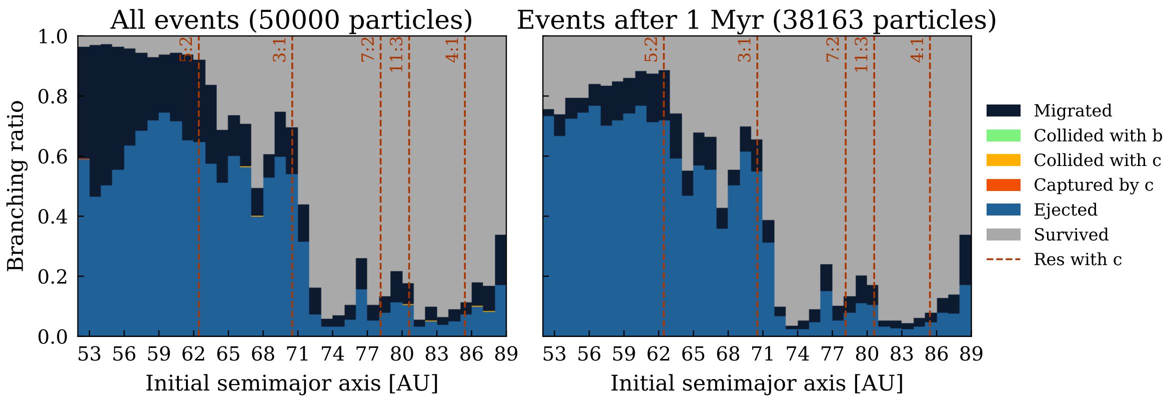

(a) Branching ratios from the outer disc simulation for the two-planet case. When excluding the first million years of simulation, the initial bins lose a large number of migrated particles, indicating that these should not be included in the calculation of migration rates, as they would skew the results.

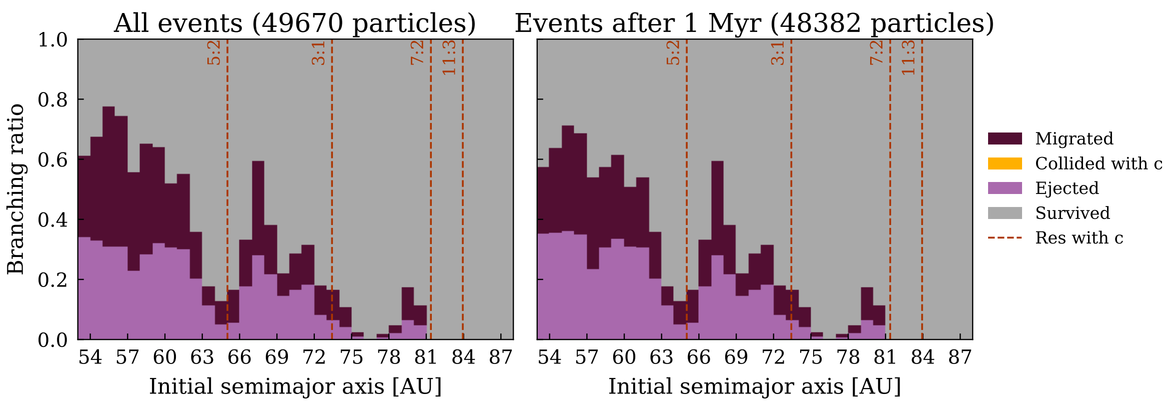

(b) Branching ratios from the outer disc simulation for the three-planet case. Here, excluding the first million years has little influence on the branching ratios and the fractions of migrated particles remain roughly the same.

Figure 4.3: Comparison of branching ratios with and without including the first 1 million years of simulation. Particles that reached $R < 18$ AU are categorised as "migrated", "ejected", "survived", "collided", and "captured", and in each bin, the sum must add up to unity. Note that the initial semimajor axes span wider than 54-87 AU. This is an artefact of the simulation, since the initial semimajor axis values are saved in the centre-of-mass reference frame, which shifts them slightly outside the original window.

a function of the particles' initial semimajor axis. The plot compares the branching ratios for all particles and for events excluding those that occurred in the first 1 million years. I do not exclude more than this since the statistics would be poor, particularly in the two-planet case, where the migration and ejection rates drop more drastically. Once again, the two different planet configurations are shown. Considering first the two-planet case, figure 4.3a, it is clear that particles that migrated within the first million years were the ones closest in (i.e., closest to the massive outer planet). This region is cleared very quickly, and particles are more likely to become scattered (both inwards and outwards) than remain in this region. After the first 1 million years, particles are still more likely to be ejected than stable, but the probability of inwards scattering decreases substantially. This is likely because the assumed criterion for a particle to become ejected is that it must have a semimajor axis above 200 AU as well as an eccentricity above 1. This is generally harder to achieve, since the distance the particle must travel to become ejected is much greater than the distance it must travel to become migrated. This explains why the migration rate peaks earlier than the ejection rate. Particles in the outer regions of the outer disc, on the other hand, evolve at later times, and the statistics in these regions remain unchanged. In the three-planet case, as shown in figure 4.3b, the difference between including or excluding the first 1 million years of events is much less. Migration is a more steady-state process, and the exclusion of particles that do so early on does not have a significant effect on the percentage of migrated particles. This is likely due to the lower mass of PDS 70 c (see table 3.2 versus table 3.1).

Interestingly, figure 4.3a shows a region of stability around $73 - 74$ AU. This roughly corresponds to the region of peak dust emission described in section 1.4. There is a similar dominance of "survived" particles around 76 AU in the three planet case. One way this may be explained is by resonances with the planets, which, as explained in section 2.2.3, could lead to stability or instability. In Jaworska et al. 2026, low-order resonances with the outermost planet in the β Pictoris system quickly clear the region of particles, which mostly become ejected. In Wallace et al. 2021, planetesimals located near a 3:1 resonance with a giant planet are in a local minimum of collision rates, whereas those near a 2:1 resonance with the planet are in a local maximum of collision rates. To test the effect of resonances in PDS 70 , some resonances with the outermost planet are overplotted in figure 4.3. It can be seen that, in the two-planet case (in figure 4.3a), between resonances, the fraction of "survived" particles is larger than near the resonances. This is particularly visible between the 5:2 and the 3:1 resonances, as well as between the 3:1 and the 7:2. In figure 4.3b, the opposite occurs. For example, the 5:2 resonance with the outer planet lies within a region of stability. It is important to note that the resonances are calculated based on the initial planet semimajor axes. Since these branching ratios are derived from multiple simulations, in which each planet may oscillate in its orbit, the resonance locations will change slightly from simulation to simulation (usually around 2 % or less), making the locations marked in figure 4.3 approximate.

4.2.2 Inclinations

The next step is to verify whether the planetesimals that cross the gap could be visible transiting the star by reaching high enough inclinations. The inclination of the disc with respect to the plane of the sky is 51.7° (Keppler, Benisty, et al. 2018). To be observed as transits, particles would have to have inclinations larger than the disc inclination with respect to our line of sight. That is, they must be inclined above $90° - 51.7° = 38.3°$ to be observable transiting. Figure 4.4a shows the inclination as a function of semimajor axis for each particle at the time it is registered as within the 18 AU inner disc. In both the two- and three-planet cases, this happens very rarely. Only about 0.14% of particles reach inclinations above 38.3°. This is due to the chosen criterion for classifying a migrated particle. A highly inclined particle will have a high z above the disc, making it no longer fulfil the criterion of a migrated particle ($\sqrt{x^2 + y^2 + z^2} < 18$ AU). To understand the importance of the choice of migration criterion, I performed the same simulations, with 10000 particles, but counted migrated particles as those with periastron distance $(a(1 - e)) < 18$ AU. This led to a drastic increase in the fraction of particles crossing the disc at high inclinations, as shown in figure 4.4b. In the two-planet case, about 11% of migrated particles enter the disc at inclinations above the disc inclination with respect to the line of sight. This is about 2% of the total number of simulated particles. As for the three planet case, the percentage of highly inclined migrating particles is 4.5%, which is a total of 0.65% of all initial particles. This factor is not as large for the three-planet case due to the low planetary masses, which lead to less violent interactions. The caveat with this criterion is that particles can be flagged as migrated when at large distances R from the star, outside the planets' orbits. This means that, even if their calculated periastron distance is less than 18 AU, their orbits may change as they move inwards and interact gravitationally with the planets.

On the other hand, the choice of migration criterion only weakly influences the fraction of all particles that migrate inward. From the cumulative distributions in figure 4.2, one can see that roughly 15% and 14% of all particles in the two- and three-planet configurations, respectively, end up migrating inward by the end of the simulation. When the periastron-based migration criterion is adopted, the fraction of migrated particles increases to 19.5% in the two-planet setup, while it remains around 14% in the three-planet case. In both cases, particles that are highly inclined may eventually undergo an alteration in their orbital parameters, bringing them closer to the disc plane and leading them to be counted as migrating.

These results show the efficiency with which high inclinations can be achieved, but they do not make

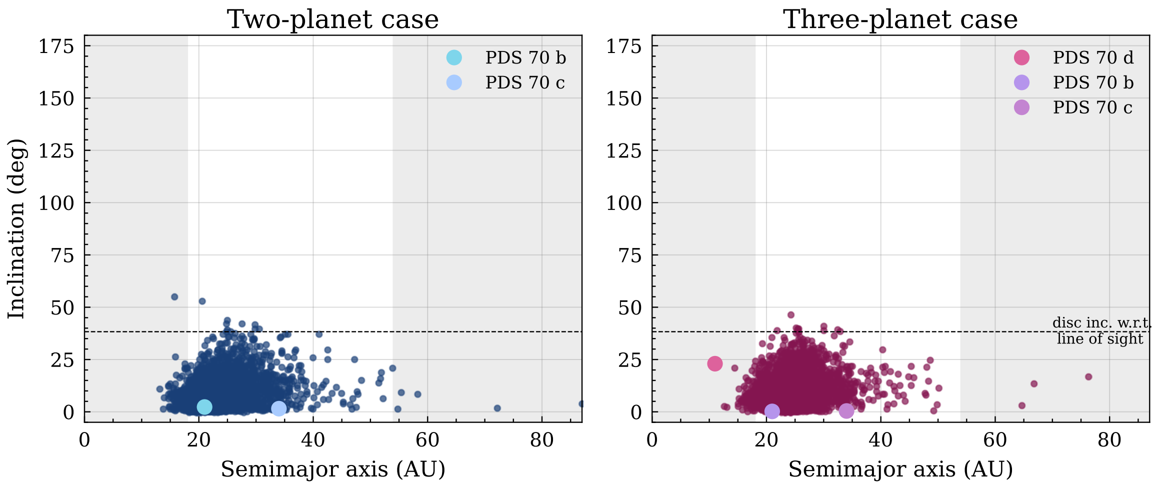

(a) Inclinations of migrated particles, where a particle is counted as migrated when $R < 18$ AU. Particle counts are 7638 and 6969 in the left and right panels, respectively.

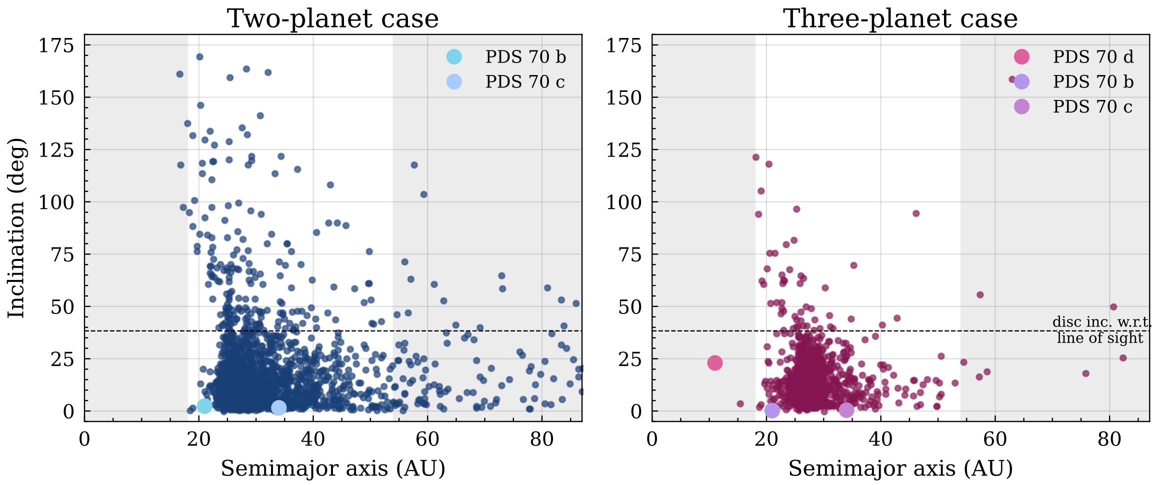

(b) Inclinations of migrated particles, where a particle is counted as migrated when $a(1-e) < 18$ AU. Note that the statistics are lower here: 1955 particles in the left panel and 1180 in the right.

Figure 4.4: Inclination distribution of particles at the moment they cross the gap as a function of semimajor axis. Grey regions indicate the inner and outer discs. The two panels show the difference that the criterion for detecting migrating particles can have. The differences between the two planet cases are more noticeable in the bottom two panels, where the higher-mass planets in the two-planet simulation lead to more particles becoming scattered above 38.3°.

the simulations comparable to exocomet observations. Firstly, it is not expected that particles at semimajor axes of 18 and above would be observable - these results serve as a preliminary proof of concept. Additionally, the orbits of these objects are very likely to change over time due to their proximity to the planets. An evaluation of their orbits within the inner disc is necessary to understand the possible inclinations star-grazing particles may achieve, and this is done in section 4.3.

4.3 Simulating the inner disc

Once it was confirmed that particles can cross the gap carved by the planets, further simulations were performed on those that reached $R < 18$ AU, both with and without gas drag, for three different particle

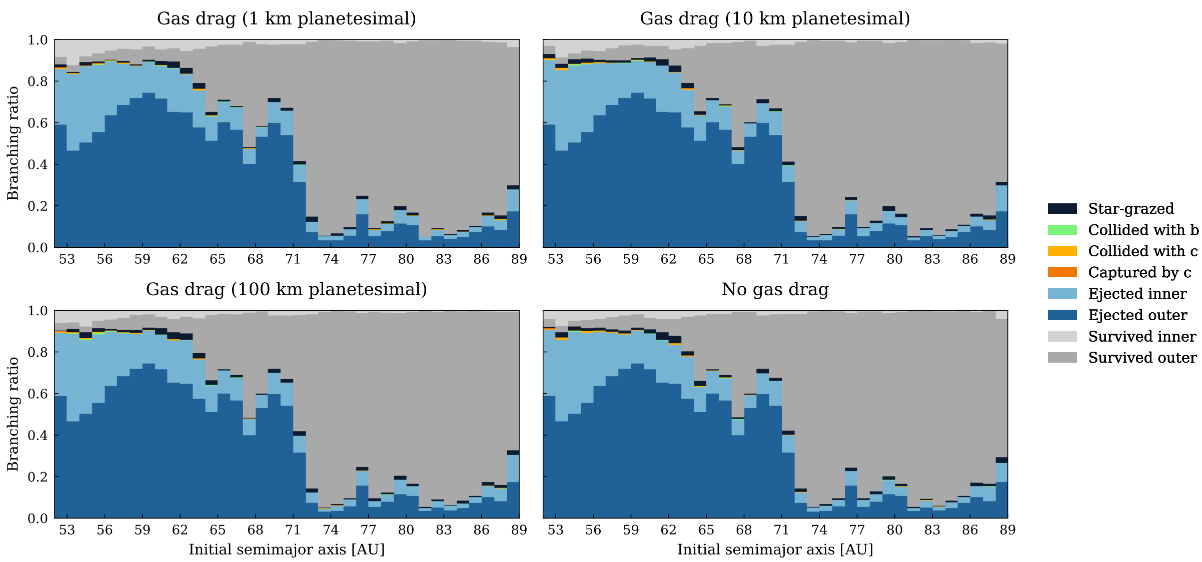

(a) Branching ratios from the outer and inner disc simulations for the two-planet case.

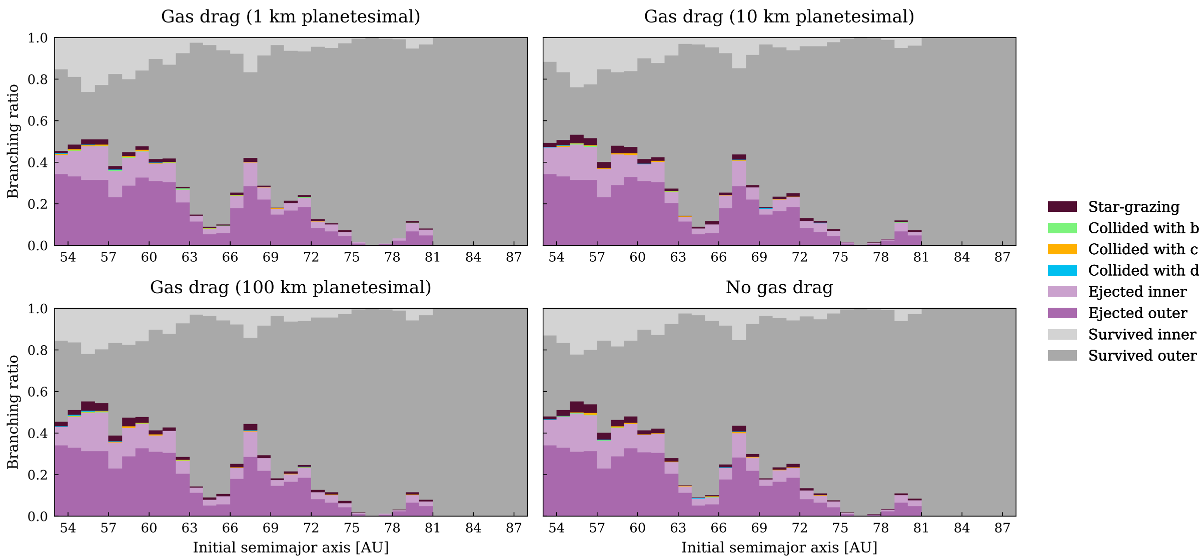

(b) Branching ratios from the outer and inner disc simulations for the three-planet case.

Figure 4.5: Distribution of particles initialised in the outer disc. "Survived" particles are simulated for 5 million years in the outer disc and 1 million years in the inner disc. Particles with other fates are simulated until the time that fate is reached, and then they are deleted. The inner disc simulations were performed four times for the same particle by using gas drag with four different planetesimal radii and excluding gas drag, for each of the planet scenarios. The outer and inner labels refer to when that even occured (before or after crossing the gap, respectively). From these plots, it can be concluded that the inclusion of gas drag and the variation of planetesimal sizes have only a small effect on the outcomes of particles. The fraction of star-grazing particles is lowest for the 1 km planetesimals, but similar for the other three cases.

sizes. Figure 4.5 shows the distribution of particle fates (branching ratios) after both the outer- and inner-disc simulations combined, as a function of their initial semimajor axis. A zoom-in of the first few bins can be found in figure A3 for the two- and three-planet cases, where the fates that are less-represented are more easily seen. The labels "outer" and "inner" refer to whether the particle reached that fate in the outer disc simulation or after it crossed 18 AU (in the inner disc simulation). This differentiation was not done for collided or captured particles due to the low statistics of this particular outcome.

Figure 4.5 compares simulations with planetesimals of 1, 10, and 100 km radii, as well as without a gas drag force (see the appendix for a zoom-in of the first few bins). Comparing first the two-planet scenarios in figure 4.5a, the differences among the three cases in the production of star-grazers are slim, albeit existent. Out of 50000 particles initially, about 1.27 % of them become star-grazers in the case of a 1-km-sized planetesimal. This value increases slightly to 1.42 % for the 10-km-sized planetesimal and 1.44 % for the 100-km-sized planetesimal. It can also be seen from figure 4.5a that the first few bins have fewer star-grazing particles in the 1-km case and a higher fraction of particles surviving in the inner disc. For example, the 53-54 AU bin has very few star-grazers in the 1 km case compared to the other three cases, and surviving particles replace them instead. This means that some particles may have spent enough time in the gas disc's high-density regions to circularise and prevent further inward scattering. This process is easier for smaller planetesimals, as inferred from figure 2.5.

In the three-planet case, shown in figure 4.5b, the difference between the panels is more apparent. The percentages of star-grazers relative to the total number of particles are 0.84%, 1.26%, and 1.33% for the 1, 10, and 100 km cases, respectively. As with the two-planet case, the 1-km-sized particles are the least likely to become star-grazers, as expected. Captures are even more unlikely in these simulations due to the lower planetary masses, but collisions with all three planets still occur.

Overall, the differences between the three planetesimal size cases are small, indicating that the gas density is not high enough in the regions where particles become star-grazers to influence this outcome, that is, around $R = 5$ AU. From figure 2.5, the stopping time at 5 AU ranges from 10^4 to 10^6 years, depending on the size of the planetesimal, but it is unlikely that particles remain in these regions for this amount of time before being flagged as star-grazers. However, the orbit of a star-grazing particle may be affected by gas drag when the particle is at or close to periastron, but at this point, it is already considered star-grazing. The aftermath of becoming a star-grazer is explored in section 4.3.1, where the planetesimal size is shown to influence particle ablation rates.

The case without gas drag is shown in the bottom right panels of figures figure 4.5a and figure 4.5b. There is a negligible difference between this case and the case with gas drag and the larger planetesimals. This can again be related to the stopping times.

The inclinations of the particles that become star-grazers, in both planet cases, are shown in figure 4.6. It can be seen that, for all planetesimal sizes, a large fraction of the total star-grazers have high inclinations (above 38.3°). For the two-planet case, shown in figure 4.6a, the percentages of particles that become star-grazing with inclinations above the disc inclination with respect to the line of sight are 41.8 %, 41.0 % and 39.9 % for the 1, 10, and 100 km cases, respectively. This shows the effect of multiple interactions with the planets and indicates the likelihood that planetesimals will be kicked out of the disc onto orbits where they could be detected from Earth. In the three planet case, see figure 4.6b, the percentages of star-grazers with high inclinations are 43.5 %, 40.6 % and 39.1 % for the 1, 10, and 100 km cases, respectively. Note that there are significantly fewer star-grazers in the three-planet-1-km case (about 2/3 as many as the other two cases). Even so, these particles have a narrower distribution of semimajor axes (meaning lower eccentricities), which could be evidence of circularisation due to gas drag. From figure 4.6, it is apparent that even for the case of 1-km planetesimals, which feel the effects of gas drag most strongly, high inclinations can be reached. In fact, in both planet configurations, the 1 km planetesimals are the most inclined population. This is particularly true for the three-planet case, which might be due to the high inclination of PDS 70 d. Particle inclinations and their evolution are discussed in more detail in the next section (section 4.3.1).

4.3.1 Ablation of star-grazers

The total ablation of a particle can be found by integrating the ablation per timestep in its orbit, as described in section 3.4.3. This rate depends strongly on a particle's position in its orbit. It is also dependent on each particle's orbital parameters. In particular, the inclination, eccentricity, and semimajor axis will determine how much time each particle will spend in an environment of high temperature and gas density. Figure 4.7 shows the predicted ablation that 1-km-sized particles would undergo as a function of their

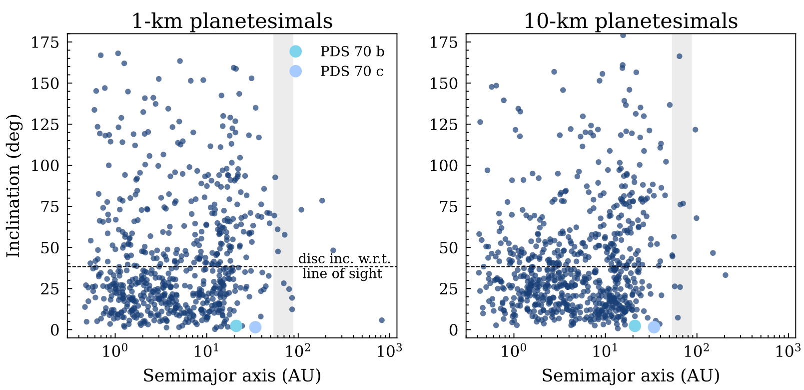

(a) The two-planet case.

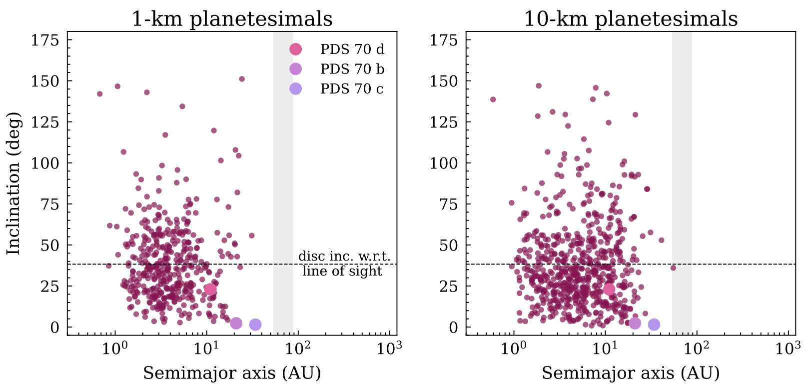

(b) The three-planet case.

Figure 4.6: Inclinations of star-grazing particles at the time of star-grazing. The results are from the simulation with gas drag and planetesimal sizes of 1, 10, and 100 km, from left to right. The figure also shows the approximate position and inclination of the planets. These are approximate, since each simulation yields slightly different orbital solutions that vary not only from simulation to simulation but also over time. The grey shaded area indicates the boundary of the inner disc. This shows that, regardless of the planetesimal size, the gas drag at the location where particles are flagged as star-grazers is not strong enough to circularise orbits (due to the spread in semimajor axes), and that particles can become inclined in all cases.

orbital phase, that is, where in their orbit they are located. To be able to make comparisons, the only parameter changed between curves is inclination. Each curve represents a particle with a constant eccentricity of 0.94 and a semimajor axis of 6 AU, which are the median values for the star-grazers produced in the two-planet simulations. In practice, the curves for simulated particles will differ in shape depending on their orbital parameters. A particle at a phase of 0° and 360° is at periastron, and at a phase of 180° is at apoastron. The total ablation is an integration over this orbit. The plot includes inclinations from 0 to 180°. These refer to the inclinations of the particle with respect to the disc, which is assumed to have an inclination of zero. At $i = 90°$, particles spend the least amount of time in the disc and enter it perpendicular to the plane of the disc. Their ablation rates will be lower than those of a particle with the same e and a but lower inclination. Above 90°, particles move in a retrograde orbit. At 180°, particles are within the plane of the disc, but due to their retrograde orbits, the relative velocity between the particle and the gas at the particle's location is different to that of their $i = 0$ degree counterparts, as shown in the right panel of figure 4.7. In both panels of the figure, the ablation rate and relative velocity drop to zero for particles of intermediate inclinations near periastron, and then shoot back up at periastron. This can be explained by the density profile shown in figure 2.3. Inclined particles at low periastron (in this case, around 0.36 AU) will not feel the disc gas, even at relatively low inclinations. As soon as they enter the disc again (say, at periastron), their ablation rates and relative velocities will jump to the highest recorded values throughout the orbit, since this is where the gas density is highest.

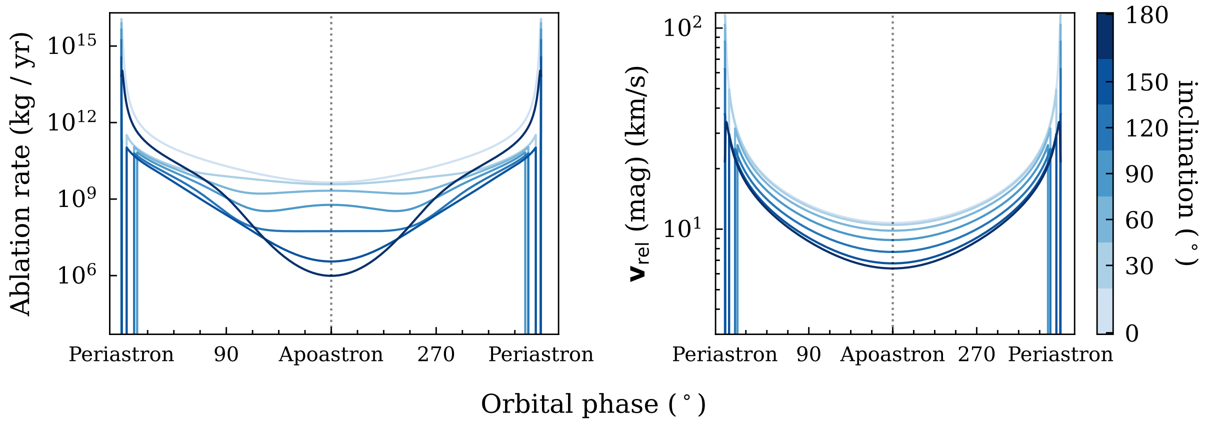

Figure 4.7: Left panel: model of ablation as a function of phase, where 0° is periastron and 180° is apoastron. Each plotted particle is 1 km in radius, has a semimajor axis of 6 AU, and an eccentricity of 0.94, matching the median values of star-grazers in the two-planet simulations. The difference between each curve is due only to the inclinations. Ablation is highest at periastron, where the particles are closest to the star and have the highest temperatures. Dips in the ablation rate correspond to regions where the gas density is essentially zero (see figure 2.3), and the ablation rate is also calculated to be zero. Right panel: relative velocity calculated as the difference between the planetesimal's velocity vector and the gas's.

With the ablation rate predictions from figure 4.7 and figure 3.3, we can proceed to the analysis of results from real simulated planetesimals. Figure 4.8 shows the total mass ablated in one orbit for the three different particle cases and two planet cases, as well as the number of orbits a particle will undergo before full ablation. Among the three sizes, smaller particles lose less mass overall. However, they are also the least massive ones. In both planet configurations, the 1-km particle median of the distribution of total mass ablated per orbit is $\sim 10^{13}$ kg. This is one order of magnitude higher than the mass of a 1-km icy particle (assuming its density is that of water, 1 $\mathrm{g/cm^3}$), meaning these star-grazers may not even survive one single orbit without becoming completely ablated. Similarly, 10-km-sized particles, with a total mass of 10^{15} kg, have a median ablation distribution that peaks around the same order of magnitude. Most of the largest particles, at 100 km, would need to complete more than 10 orbits before fully ablating, since their total ablation peaks around 10^{17} kg while their total mass is $\sim 10^{18}$ kg. The tails of the distributions present mostly in figure 4.8a likely represent particles that spend very little time within the disc and have inclinations near 90°. They are also likely highly eccentric, resulting in a faster periastron passage and less interaction with the disc. The distributions are more narrow in the three-planet case (see figure 4.8b), consistent with figure 4.6, which shows a smaller spread in semimajor axes for the star-grazers in the three-planet simulations compared to those of the two-planet simulations. As in the two-planet case, it is the 100 km planetesimals that have a wider spread in total ablation. These are the particles that are less likely to become circularised, so they can have larger semimajor axes.

To better understand these distributions and the dependencies on the different orbital parameters, figure 4.9 shows the total ablation per orbit as a function of eccentricity and inclination for star-grazers. To reduce the dependency of these results on periastron distance, only star-grazers with $0.39 < a(1-e) < 0.4$ are included. In both planet cases, particles become star-grazers with a wide distribution of eccentricities (although the two-planet simulation particles are more likely to have eccentricities below 0.6 than the three-planet simulation particles). However, there is certainly a preference for star-grazers to be highly eccentric, with $e > 0.9$. This is because the criterion to become a star-grazing planetesimal depends on the periastron distance, which would include particles on highly eccentric orbits, since the range of semimajor axes that they can have to fulfil this criterion is larger. There is also a correlation between inclination and total ablation. Looking at the highly eccentric particles ($e > 0.9$), these have a wide range of possible ablation rates, and the lowest rates recorded are for particles of inclinations around 90°, which spend the least amount of time interacting with the disc. For eccentricities between 0.2 and 0.9 (or 0.6

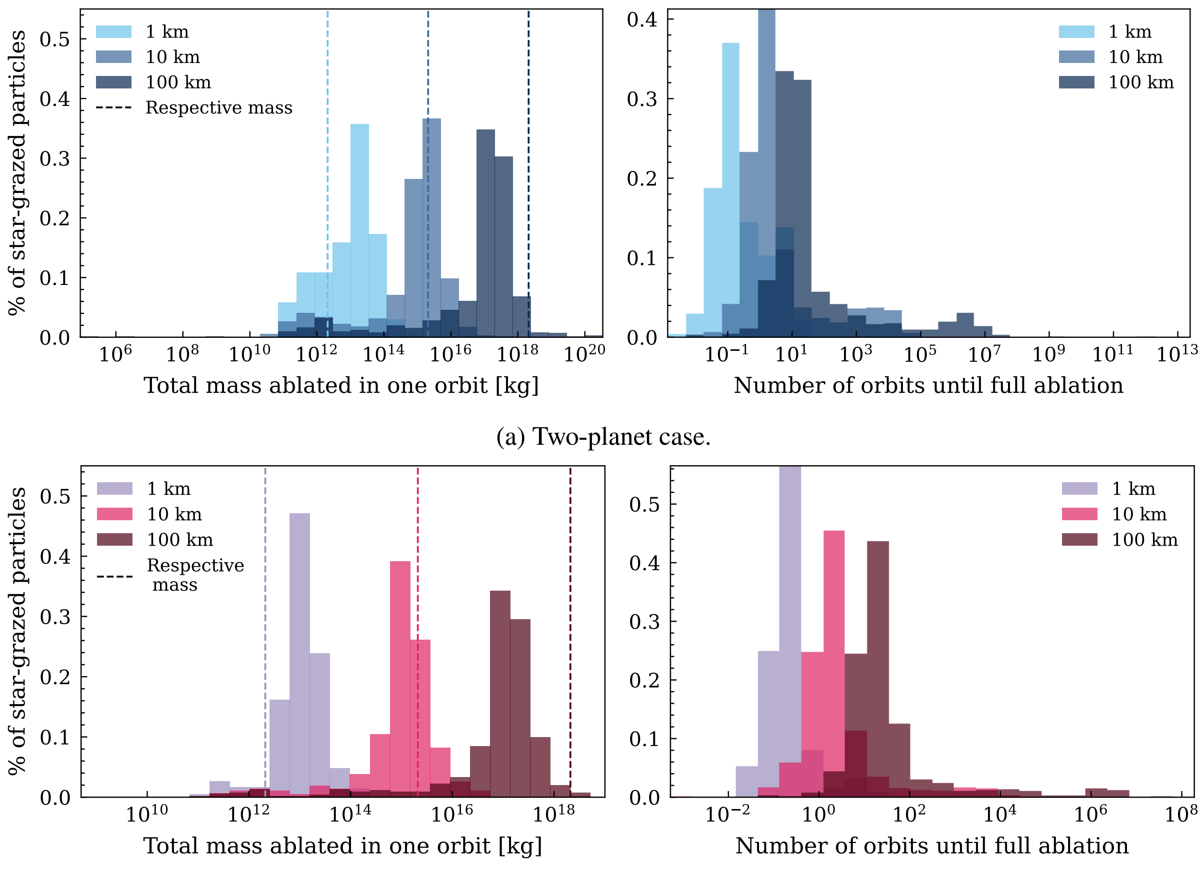

(a) Two-planet case.

(b) Three-planet case.

Figure 4.8: Left: total mass ablated in one orbit for the population of star-grazing particles. Each planetesimal size is shown, along with the mass of a planetesimal of that size. Right: number of orbits that particles undergo before becoming fully ablated. The figure shows that star-grazing planetesimals have high ablation rates. Most 1 km and 10 km planetesimals ablate fully within one orbit. On the other hand, the larger planetesimals of 100 km ablate after 10 or more orbits.

and 0.9 in the three-planet case) and for each planetesimal size, particles with similar inclinations have similar total ablations, and there is a clear layered structure of low-inclination particles at higher total ablations and vice versa. The masses of each planetesimal, calculated from its radius, are overplotted as dashed lines. The statistics from figure 4.8 are also recovered here - the majority of 1-km particles lie above their mass line, most 10-km particles lie on top of their mass line, and 100-km particles tend to lie just below their mass line.

The ablation rate calculations do not account for how mass loss will reduce the planetesimal's size and, consequently, the ablation rate, throughout the orbit. However, it can be assumed that ablation is a runaway process, such that once it begins, the smaller a planetesimal becomes, the higher the fraction of its total mass it loses. This can be seen in the right-hand side panels of figure 4.8, where the number of orbits until full ablation is smallest for the 1-km planetesimals compared to the 10- and 100-km ones.

Given that planetesimals have generally much lower inclinations at the moment of gap crossing (figure 4.4a), it would be interesting to understand at which point in their orbit they become inclined. This is because, if high inclinations are reached when the particle is already at low periastron, there is a chance it would have become fully ablated before even becoming classified as a star-grazer. Particle inclinations as a function of periastron distance are shown in figure 4.10 for a few examples of particles that become star-grazers in all three simulations of different planetesimal sizes (from the two- and three-planet simulations). These particles are also chosen such that they reach inclinations above 30° before their periastron

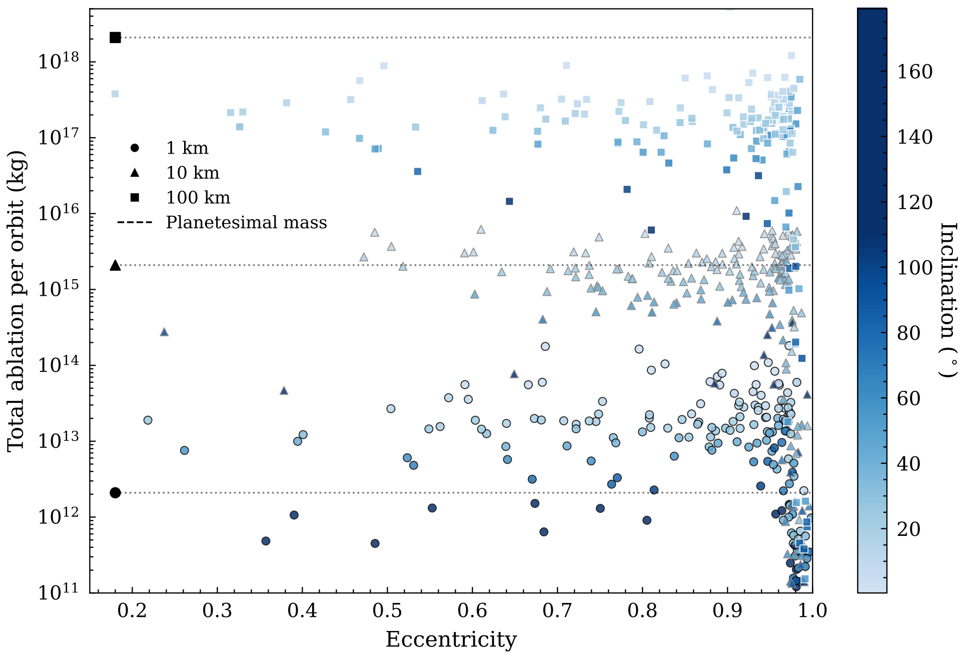

(a) Two-planet case.

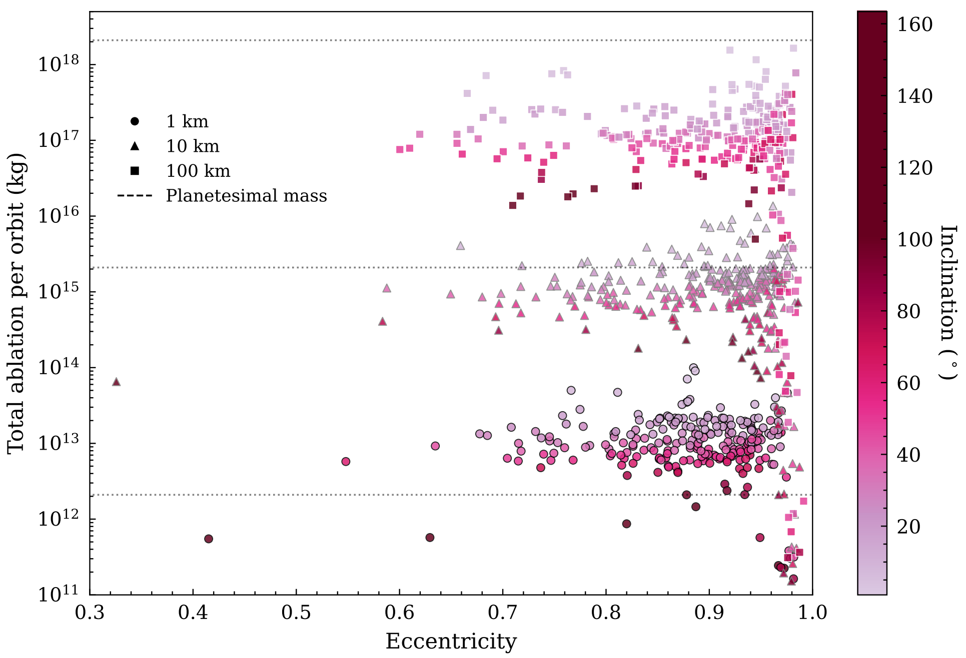

(b) Three-planet case.

Figure 4.9: Total ablated mass per orbit as a function of eccentricity for star-grazers in both planet configurations. The three planetesimal radii are shown as differently shaped markers, with different outline colours (white-outlined squares, grey-outlined triangles, and black-outlined circles). The colorbar (shape fill) indicates the inclination, with darker colours indicating higher inclinations. To minimise the dependency on periastron, all particles have periastrons between 0.39 AU and 0.4 AU. The plot shows that most star-grazers are highly eccentric (> 0.9) and that the total ablation per orbit varies little with eccentricity (per planetesimal size) when $e < 0.95$, but for higher eccentricities, particles with inclinations close to 90° feel significantly less ablation. This is because the little time spent in the disc occurs at periastron, and because of their high eccentricity, this passage is exceptionally short. The dashed lines indicate the mass corresponding to each planetesimal radius.

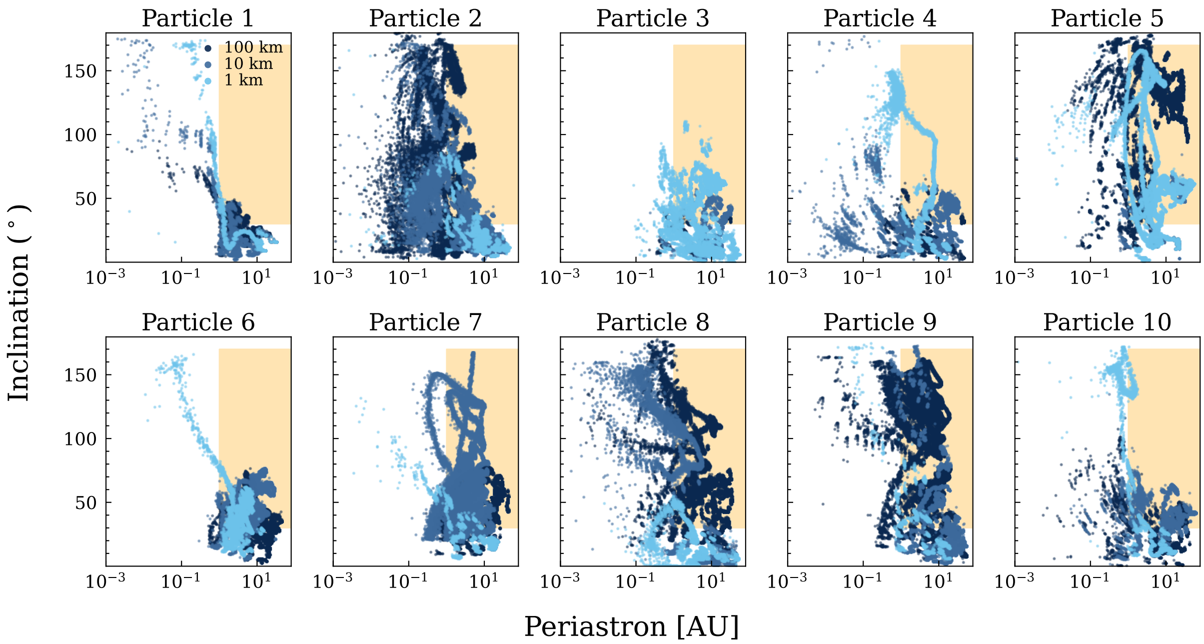

(a) The two-planet case.

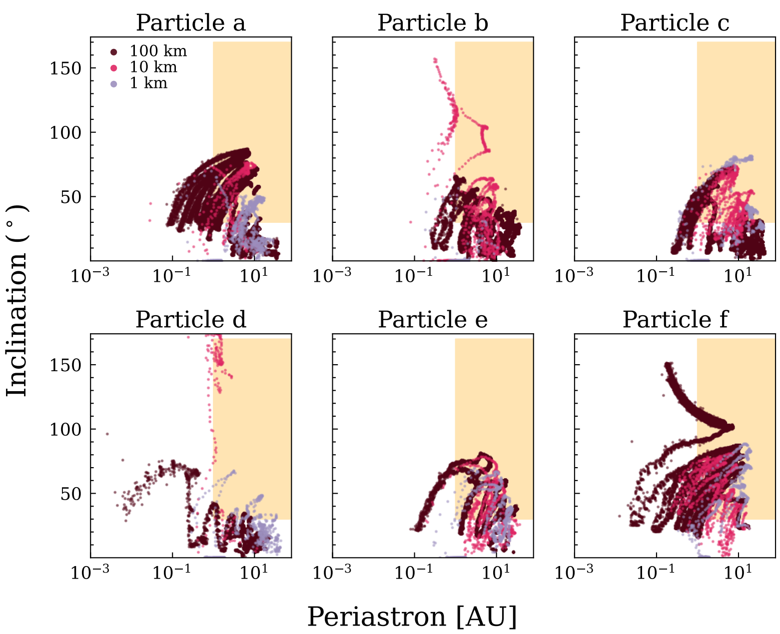

(b) The three-planet case.

Figure 4.10: Inclinations of star-grazing particles as a function of periastron distance over their entire time in the inner disc. Each panel shows the evolution of a particle with three different planetesimal sizes, and particles were chosen so that each simulation for each size would lead to a star-grazing particle. It was also guaranteed that particles did not reach a periastron below 1 AU before reaching an inclination above 30°. The shaded region is an approximate "safe zone", where particles can likely spend multiple orbits before becoming fully ablated. It is delimited by periastrons above 1 AU and inclinations between 30 and 175°. The plot shows examples of particles that spend several orbits within this region, meaning that it is possible for particles to reach high inclinations before reaching low periastrons, where they would fully ablate.

is 1 AU, in all three of the planetesimal sizes. A shaded area is marked in each panel indicating a "safe zone". This is a region where particles can likely spend several orbits without becoming fully ablated and is delimited by periastrons above 1 AU and inclinations between 30 to 175°. These criteria are rough estimates based on the ablation rates of star-grazing particles and the inclination dependencies presented in figure 4.7. In this plot, the particle at 30° inclination has an ablation rate almost 4 orders of magnitude lower at periastron. These results show that some star-grazers can reach high inclinations while still at larger periastrons (> 1 AU), meaning they would not be ablated before being classified as star-grazers. However, only the most inclined star-grazers would survive for several orbits. The criteria used to find these particles are constraining; it is particularly rare that the same particle becomes a star-grazer in all three of the planetesimal size simulations. Since the simulations are independent of each other, this limiting requirement could be removed, and one would obtain a significantly higher outcome of particles that enter the "safe zone".

Chapter 5

Conclusions & Outlook

In this thesis, I have simulated the PDS 70 planets and planetesimals in the protoplanetary disc to answer a series of questions about their evolution. First, I studied the system's stability with two and three planets to understand the effects of different planetary masses. From this, I learned that in the two-planet case, it is most likely that the outermost planet is more massive than the innermost planet. I find that the most probable configurations for stability agree with the literature and give a mass of $1-3M_{\mathrm{Jup}}$ for PDS 70 b. The mass of PDS 70 c could not be properly constrained from dynamical simulations alone. As for the three-planet case, I found that PDS 70 d, if it exists, likely has a mass below $1M_{\mathrm{Jup}}$. In future simulations, it would be interesting to test the addition of more planets in the inner system, such as lower-mass terrestrial planets, to understand their effect on the stability of the system. One could also explore the placement of planets in mean-motion resonances and evaluate whether this would allow for stability with larger planetary masses.

In my simulations of a protoplanetary disc, I found that in both the two- and three-planet cases, particles are able to cross the gap carved by the planets and do so at varying rates. The migration rates in the last 1 million years of a 5-million-year simulation are about 5 times larger in the three-planet case. However, this is highly dependent on the planet masses and initial setup, since in the two-planet case, most of the migration occurs in the first million years due to the influence of the more massive planets. Most particles that migrate originate near the inner edge of the outer disc (54 to 60 AU). The outer regions of this disc (75 AU onwards) lead to mostly stable particles that do not get ejected or migrate. Future simulations may run for more than 5 million years to understand whether these stability regions are truly stable or if they simply take longer to evolve.

Simulating the migrated particles further in the inner disc, I tested a gas drag force assuming particles of three different sizes - 1, 10, and 100 km. Smaller particles are influenced more by this force than larger particles. When it comes to the final outcome of particles, in particular, the total fraction of particles that become star-grazers, gas drag does not have an influence on the large particles (10 and 100 km). However, it does reduce the likelihood of 1 km planetesimals becoming star-grazing as they are more easily circularised by the gas. Gas drag does not prevent particles from reaching high inclinations ($>38.3°$), where they could be visible as transits. However, the gas in the disc has a significant effect on particle ablation. Low-inclination star-grazers will most likely be completely ablated within a single orbit (for 1 km and 10 km particles) or a few orbits (for 100 km particles). The ablation rate is highest at periastron, meaning these icy particles will deposit most of their water content in these inner regions. It is also possible that planetesimals reach high inclinations before entering the regions where ablation is strongest. These particles would fit the profile of exocomets that can complete several orbits around the star. Future simulations may be set up to calculate the ablation rate at each timestep, to understand at what point in a planetesimal's orbit it begins to play a significant role and how the mass loss influences the effect of gas drag.

Although the simulations presented in this thesis cannot be directly compared to observations, the results support observational findings of the PDS 70 system (Novais et al. 2025; Perotti et al. 2023).

The simulations produce exocomets on highly eccentric and inclined orbits, similar to those inferred from the variable absorption features attributed to exocomets transiting the PDS 70 star (Novais et al. 2025). Furthermore, the inward transport of water-rich material shown in the simulations provides a plausible mechanism for delivering volatiles to the inner disc, supporting interpretations that icy bodies may contribute to the material observed near the star. While the present work does not predict directly observable quantities, it demonstrates that the dynamical pathways required to explain the abovementioned observations can arise naturally within the simulated planetary architecture.

Appendix A

Appendix

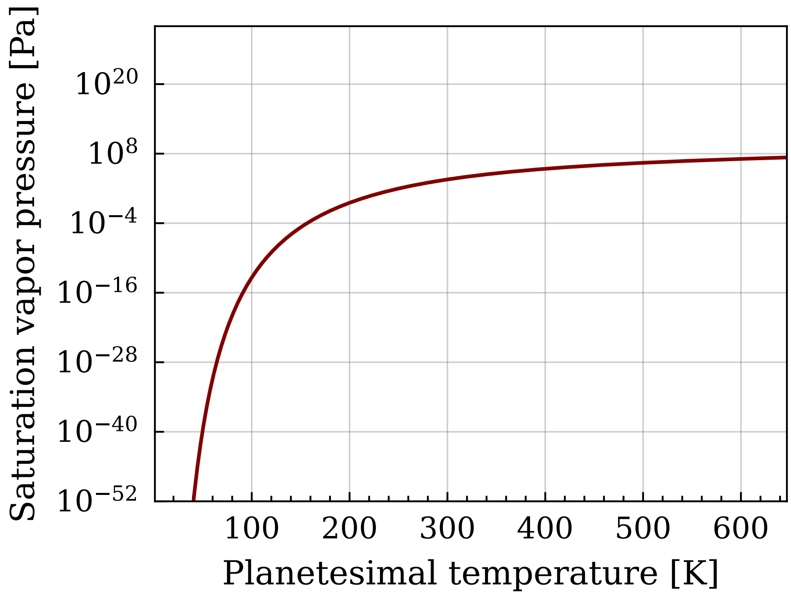

Figure A1: Saturated vapour pressure of water.

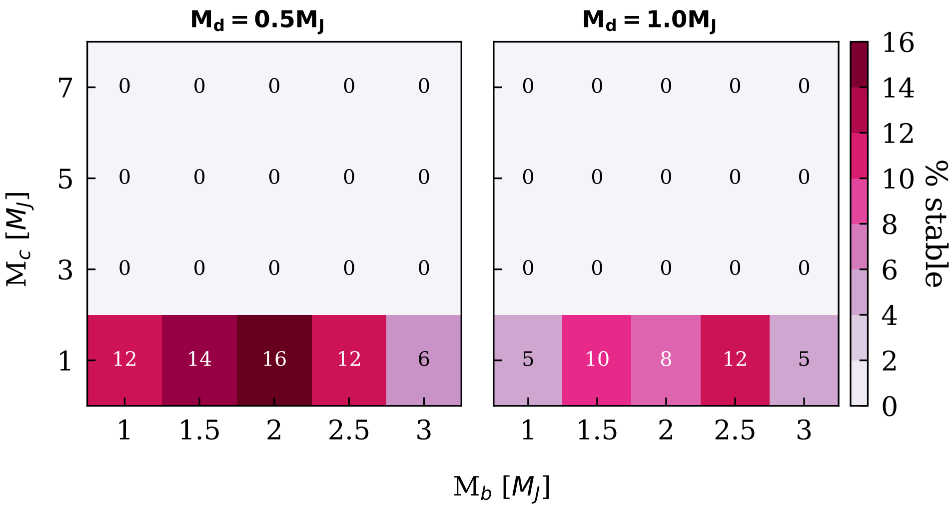

Figure A2: Planets starting with semimajor axes of 12.9, 20.5, and 32.4, forcing a period ratio of 1:2:4.

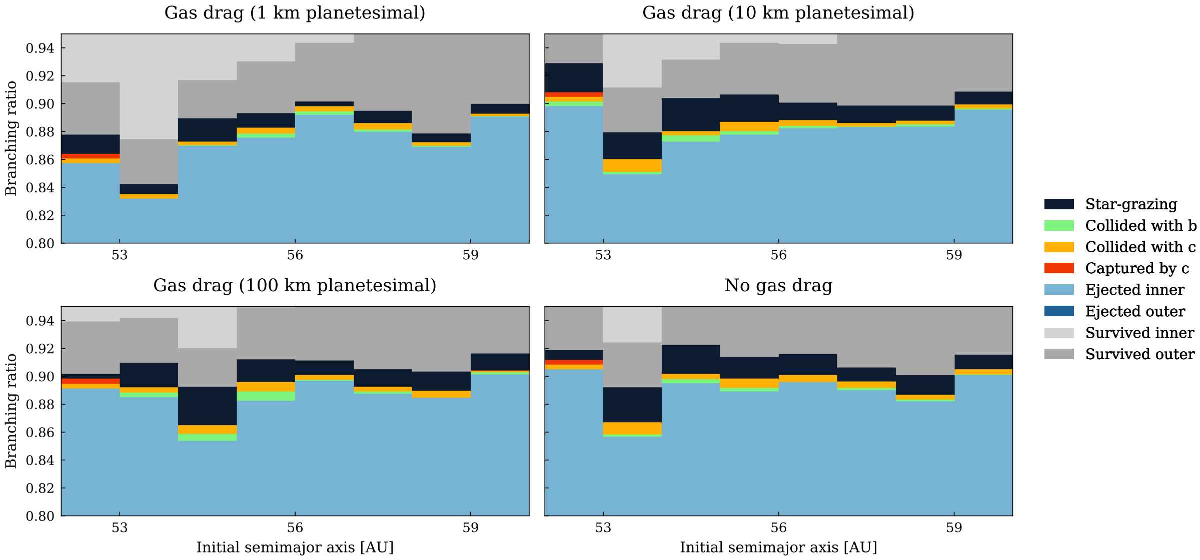

(a) Two-planet case.

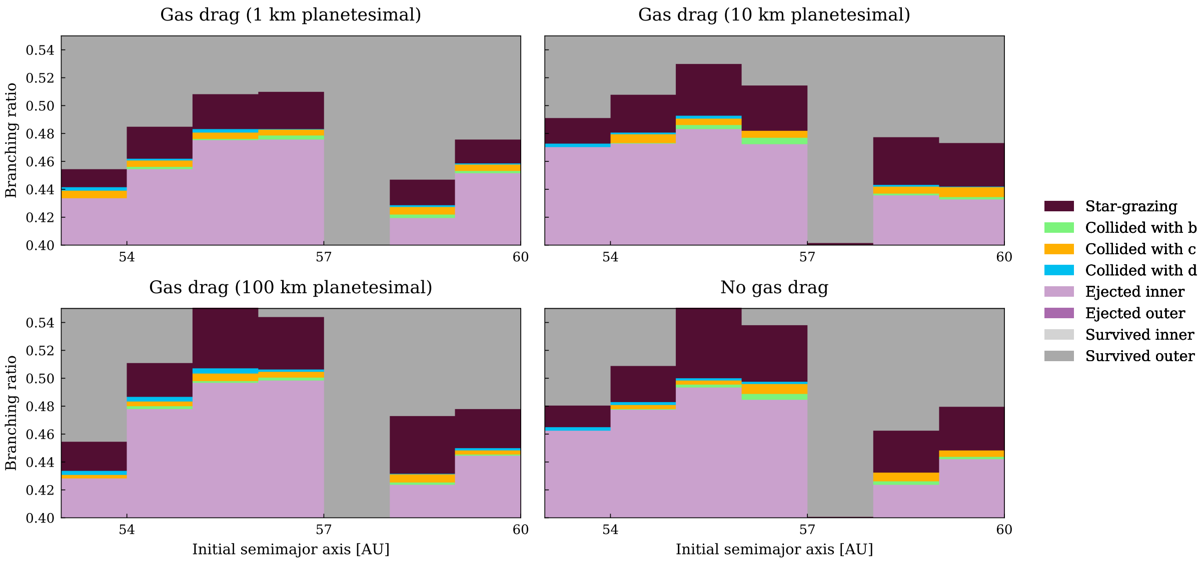

(b) Three-planet case.

Figure A3: Zoom-in of the branching ratios in figure 4.5 to better show the fractions of collided, captured, and star-grazing particles in the first few bins.

Bibliography

Alencar, S. H. P. et al. (Apr. 2000). “Profiles of Strong Permitted Lines in Classical T Tauri Stars”. In: *The Astronomical Journal* 119. ADS Bibcode: 2000AJ....119.1881A, pp. 1881–1900. ISSN: 0004-6256. DOI: 10.1086/301300. URL: https://ui.adsabs.harvard.edu/abs/2000AJ....119.1881A.

Ambartsumian, V. A. (Jan. 1947). *The evolution of stars and astrophysics*. Publication Title: Évolyutsiya zvezd i astrofizika ADS Bibcode: 1947esa..book.....A. URL: https://ui.adsabs.harvard.edu/abs/1947esa..book.....A.

Andrews, S. M. et al. (Apr. 2011). “RESOLVED IMAGES OF LARGE CAVITIES IN PROTOPLANETARY TRANSITION DISKS”. en. In: *The Astrophysical Journal* 732.1, p. 42. ISSN: 0004-637X. DOI: 10.1088/0004-637X/732/1/42. URL: https://doi.org/10.1088/0004-637X/732/1/42.

Appenzeller, I. et al. (Sept. 1989). “T Tauri stars”. en. In: *The Astronomy and Astrophysics Review* 1.3, pp. 291–334. ISSN: 1432-0754. DOI: 10.1007/BF00873081. URL: https://doi.org/10.1007/BF00873081.

Bae, J. et al. (Oct. 2019). “An Ideal Testbed for Planet–Disk Interaction: Two Giant Protoplanets in Resonance Shaping the PDS 70 Protoplanetary Disk”. en. In: *The Astrophysical Journal Letters* 884.2, p. L41. ISSN: 2041-8205. DOI: 10.3847/2041-8213/ab46b0. URL: https://dx.doi.org/10.3847/2041-8213/ab46b0.

Bendahan-West, R. et al. (Jan. 2025). “Quantifying spectroscopic Ca II exocomet transit occurrence in two decades of HARPS data”. en. In: *Monthly Notices of the Royal Astronomical Society* 537.1, pp. 229–251. ISSN: 0035-8711, 1365-2966. DOI: 10.1093/mnras/stae2804. URL: https://academic.oup.com/mnras/article/537/1/229/7931869.

Benisty, M. et al. (July 2021). “A Circumplanetary Disk around PDS70c”. In: *The Astrophysical Journal Letters* 916.1, p. L2. ISSN: 2041-8205, 2041-8213. DOI: 10.3847/2041-8213/ac0f83. URL: https://iopscience.iop.org/article/10.3847/2041-8213/ac0f83.

Benner, L. A. M. et al. (Nov. 1995). “On the Orbital Evolution and Origin of Comet Shoemaker-Levy 9”. In: *Icarus* 118.1, pp. 155–168. ISSN: 0019-1035. DOI: 10.1006/icar.1995.1182. URL: https://www.sciencedirect.com/science/article/pii/S0019103585711827.

Beust, H., J. Milli, et al. (Mar. 2024). “Dynamics of the beta Pictoris planetary system and its falling evaporating bodies”. en. In: *Astronomy & Astrophysics* 683, A89. ISSN: 0004-6361, 1432-0746. DOI: 10.1051/0004-6361/202348203. URL: https://www.aanda.org/articles/aa/abs/2024/03/aa48203-23/aa48203-23.html.

Beust, H. and A. Morbidelli (Apr. 1996). “Mean-Motion Resonances as a Source for Infalling Comets toward β Pictoris”. In: *Icarus* 120.2, pp. 358–370. ISSN: 0019-1035. DOI: 10.1006/icar.1996.0056. URL: https://www.sciencedirect.com/science/article/pii/S0019103596900561.

Blum, J. et al. (July 2022). “Formation of Comets”. In: *Universe* 8.7. arXiv:2207.12731 [astro-ph], p. 381. ISSN: 2218-1997. DOI: 10.3390/universe8070381. URL: http://arxiv.org/abs/2207.12731.

Boyajian, T. S. et al. (Apr. 2016). “Planet Hunters IX. KIC 8462852 - where’s the flux?” In: *Monthly Notices of the Royal Astronomical Society* 457. ADS Bibcode: 2016MNRAS.457.3988B, pp. 3988–4004. ISSN: 0035-8711. DOI: 10.1093/mnras/stw218. URL: https://ui.adsabs.harvard.edu/abs/2016MNRAS.457.3988B.

Carusi, A. et al. (June 1979). “Planetary close encounters: Importance of nearly tangent orbits”. en. In: *The moon and the planets* 22.1, pp. 113–124. ISSN: 1573-0794. DOI: 10.1007/BF00896872. URL: https://doi.org/10.1007/BF00896872.

Chauvin, G. (Jan. 2024). "Direct imaging of exoplanets: Legacy and prospects". In: *Comptes Rendus Physique* 24. ADS Bibcode: 2024CRPhy..24S.139C, p. 139. ISSN: 1631-0705. DOI: 10.5802/crphys.139. URL: https://ui.adsabs.harvard.edu/abs/2024CRPhy..24S.139C.

Chen, Z. et al. (Feb. 2022). "Planetary Accretion Shocks with a Realistic Equation of State". In: *The Astrophysical Journal Letters* 925.2. arXiv:2201.07453 [astro-ph.EP], p. L14. ISSN: 2041-8205, 2041-8213. DOI: 10.3847/2041-8213/ac4ca9. URL: http://arxiv.org/abs/2201.07453.

Christiaens, V. et al. (May 2024). "MINDS: JWST/NIRCam imaging of the protoplanetary disk PDS 70 - A spiral accretion stream and a potential third protoplanet". en. In: *Astronomy & Astrophysics* 685, p. L1. ISSN: 0004-6361, 1432-0746. DOI: 10.1051/0004-6361/202349089. URL: https://www.aanda.org/articles/aa/abs/2024/05/aa49089-23/aa49089-23.html.

Davies, R. et al. (Sept. 2012). "Adaptive Optics for Astronomy". In: *Annual Review of Astronomy and Astrophysics* 50.1. arXiv:1201.5741 [astro-ph], pp. 305–351. ISSN: 0066-4146, 1545-4282. DOI: 10.1146/annurev-astro-081811-125447. URL: http://arxiv.org/abs/1201.5741.

Deeg, H. J. et al., eds. (2018). *Handbook of Exoplanets*. Springer. URL: https://doi.org/10.1007/978-3-319-55333-7.

Do Ó, C. R. et al. (Oct. 2025). *On The Orbital Evolution of Multiple Wide Super-Jupiters: How Disk Migration and Dispersal Shape the Stability of The PDS 70 System*. arXiv:2510.11021 [astro-ph]. DOI: 10.48550/arXiv.2510.11021. URL: http://arxiv.org/abs/2510.11021.

Doi, K. et al. (Oct. 2024). "Asymmetric Dust Accumulation of the PDS 70 Disk Revealed by ALMA Band 3 Observations". en. In: *The Astrophysical Journal Letters* 974.2, p. L25. ISSN: 2041-8205. DOI: 10.3847/2041-8213/ad7f51. URL: https://dx.doi.org/10.3847/2041-8213/ad7f51.

Dong, R. et al. (Dec. 2012). "The Structure of Pre-transitional Protoplanetary Disks. I. Radiative Transfer Modeling of the Disk+Cavity in the PDS 70 System". In: *The Astrophysical Journal* 760. ADS Bibcode: 2012ApJ...760..111D, p. 111. ISSN: 0004-637X. DOI: 10.1088/0004-637X/760/2/111. URL: https://ui.adsabs.harvard.edu/abs/2012ApJ...760..111D.

Duffell, P. C. et al. (Mar. 2015). "SHALLOW CAVITIES IN MULTIPLE-PLANET SYSTEMS". en. In: *The Astrophysical Journal* 802.1, p. 42. ISSN: 0004-637X. DOI: 10.1088/0004-637X/802/1/42. URL: https://doi.org/10.1088/0004-637X/802/1/42.

Edgar, R. G. et al. (Sept. 2007). "The Minimum Gap-opening Planet Mass in an Irradiated Circumstellar Accretion Disk". In: *Monthly Notices of the Royal Astronomical Society* 381.3. arXiv:0705.3436 [astro-ph], pp. 1280–1286. ISSN: 00358711, 13652966. DOI: 10.1111/j.1365-2966.2007.12305.x. URL: http://arxiv.org/abs/0705.3436.

Edwards, S. et al. (July 2006). "Probing T Tauri Accretion and Outflow with 1 Micron Spectroscopy". In: *The Astrophysical Journal* 646.1. arXiv:astro-ph/0604006, pp. 319–341. ISSN: 0004-637X, 1538-4357. DOI: 10.1086/504832. URL: http://arxiv.org/abs/astro-ph/0604006.

Eriksson, L. E. J. et al. (Apr. 2021). "The fate of planetesimals formed at planetary gap edges". In: *Astronomy and Astrophysics* 648. ADS Bibcode: 2021A&A...648A.112E, A112. ISSN: 0004-6361. DOI: 10.1051/0004-6361/202039889. URL: https://ui.adsabs.harvard.edu/abs/2021A&A...648A.112E.

Espaillat, C. C. et al. (Sept. 2021). "Measuring the density structure of an accretion hot spot". In: *Nature* 597. ADS Bibcode: 2021Natur.597...41E, pp. 41–44. ISSN: 0028-0836. DOI: 10.1038/s41586-021-03751-5. URL: https://ui.adsabs.harvard.edu/abs/2021Natur.597...41E.

Ferlet, R. et al. (Oct. 1987). "The beta Pictoris circumstellar disk. V. Time variations of the Ca II-K line." In: *Astronomy and Astrophysics* 185. ADS Bibcode: 1987A&A...185..267F, pp. 267–270. ISSN: 0004-6361. URL: https://ui.adsabs.harvard.edu/abs/1987A&A...185..267F.

Gaia Collaboration et al. (Aug. 2018). "*Gaia* Data Release 2: Summary of the contents and survey properties". In: *Astronomy & Astrophysics* 616, A1. ISSN: 0004-6361, 1432-0746. DOI: 10.1051/0004-6361/201833051. URL: https://www.aanda.org/10.1051/0004-6361/201833051.

Grady, C. A. et al. (May 2018). "The Star-grazing Bodies in the HD 172555 System". en. In: *The Astronomical Journal* 155.6, p. 242. ISSN: 1538-3881. DOI: 10.3847/1538-3881/aabe74. URL: https://doi.org/10.3847/1538-3881/aabe74.

Guillot, T. et al. (Dec. 2014). "On the filtering and processing of dust by planetesimals. I. Derivation of collision probabilities for non-drifting planetesimals". In: *Astronomy and Astrophysics* 572. ADS Bibcode: 2014A&A...572A..72G, A72. ISSN: 0004-6361. DOI: 10.1051/0004-6361/201323021. URL: https://ui.adsabs.harvard.edu/abs/2014A&A...572A..72G.

Haffert, S. Y. et al. (Aug. 2019). "Two accreting protoplanets around the young star PDS 70". en. In: *Nature Astronomy* 3.8, pp. 749–754. ISSN: 2397-3366. DOI: 10.1038/s41550-019-0780-5. URL: https://www.nature.com/articles/s41550-019-0780-5.

Hammond, I. et al. (Apr. 2025). "Keplerian motion of a compact source orbiting the inner disk of PDS 70: A third protoplanet in a resonance with b and c?" In: *Monthly Notices of the Royal Astronomical Society*. arXiv:2504.11127 [astro-ph], staf586. ISSN: 0035-8711, 1365-2966. DOI: 10.1093/mnras/staf586. URL: http://arxiv.org/abs/2504.11127.

Hartmann, L. et al. (Mar. 1998). "Accretion and the Evolution of T Tauri Disks". en. In: *The Astrophysical Journal* 495.1, p. 385. ISSN: 0004-637X. DOI: 10.1086/305277. URL: https://iopscience.iop.org/article/10.1086/305277.

Hashimoto, J., R. Dong, et al. (Sept. 2012). "POLARIMETRIC IMAGING OF LARGE CAVITY STRUCTURES IN THE PRE-TRANSITIONAL PROTOPLANETARY DISK AROUND PDS 70: OBSERVATIONS OF THE DISK*". en. In: *The Astrophysical Journal Letters* 758.1, p. L19. ISSN: 2041-8205. DOI: 10.1088/2041-8205/758/1/L19. URL: https://doi.org/10.1088/2041-8205/758/1/L19.

Hashimoto, J., Y. Aoyama, et al. (Apr. 2020). "Accretion Properties of PDS 70b with MUSE*". en. In: *The Astronomical Journal* 159.5, p. 222. ISSN: 1538-3881. DOI: 10.3847/1538-3881/ab811e. URL: https://doi.org/10.3847/1538-3881/ab811e.

Herbig, G. H. (Jan. 1962). "The Properties and Problems of T Tauri Stars and Related Objects". In: *Advances in Astronomy and Astrophysics* 1. ADS Bibcode: 1962AdA&A....1...47H, pp. 47–103. DOI: 10.1016/B978-1-4831-9919-1.50006-6. URL: https://ui.adsabs.harvard.edu/abs/1962AdA&A....1...47H.

Ida, S., T. Guillot, et al. (June 2016). "The radial dependence of pebble accretion rates: A source of diversity in planetary systems. I. Analytical formulation". In: *Astronomy and Astrophysics* 591. ADS Bibcode: 2016A&A...591A..72I, A72. ISSN: 0004-6361. DOI: 10.1051/0004-6361/201628099. URL: https://ui.adsabs.harvard.edu/abs/2016A&A...591A..72I.

Ida, S., H. Tanaka, et al. (Sept. 2018). "Slowing Down Type II Migration of Gas Giants to Match Observational Data". In: *The Astrophysical Journal* 864. ADS Bibcode: 2018ApJ...864...77I, p. 77. ISSN: 0004-637X. DOI: 10.3847/1538-4357/aad69c. URL: https://ui.adsabs.harvard.edu/abs/2018ApJ...864...77I.

Iglesias, D. et al. (Nov. 2025). *An Overview of Exocomets*. arXiv:2511.08270 [astro-ph]. DOI: 10.48550/arXiv.2511.08270. URL: http://arxiv.org/abs/2511.08270.

Jaworska, K. P. et al. (Mar. 2026). "Exocomets of β Pictoris: II. Two dynamical families of exocomets simulated with REBOUND". In: *Astronomy and Astrophysics* 708. ADS Bibcode: 2026A&A...708A..59J, A59. ISSN: 0004-6361. DOI: 10.1051/0004-6361/202556139. URL: https://ui.adsabs.harvard.edu/abs/2026A&A...708A..59J.

Johansen, A., J. Blum, et al. (Jan. 2014). "The Multifaceted Planetesimal Formation Process". In: ADS Bibcode: 2014prpl.conf..547J. eprint: arXiv:1402.1344, pp. 547–570. DOI: 10.2458/azu_uapress_9780816531240-ch024. URL: https://ui.adsabs.harvard.edu/abs/2014prpl.conf..547J.

Johansen, A., J. S. Oishi, et al. (Aug. 2007). "Rapid planetesimal formation in turbulent circumstellar disks". In: *Nature* 448. ADS Bibcode: 2007Natur.448.1022J, pp. 1022–1025. ISSN: 0028-0836. DOI: 10.1038/nature06086. URL: https://ui.adsabs.harvard.edu/abs/2007Natur.448.1022J.

Joy, A. H. (Sept. 1945). "T Tauri Variable Stars." In: *The Astrophysical Journal* 102. ADS Bibcode: 1945ApJ...102..168J, p. 168. ISSN: 0004-637X. DOI: 10.1086/144749. URL: https://ui.adsabs.harvard.edu/abs/1945ApJ...102..168J.

Kenyon, S. J. et al. (Dec. 1987). "Spectral Energy Distributions of T Tauri Stars: Disk Flaring and Limits on Accretion". In: *The Astrophysical Journal* 323. ADS Bibcode: 1987ApJ...323..714K, p. 714. ISSN:

0004-637X. DOI: 10.1086/165866. URL: https://ui.adsabs.harvard.edu/abs/1987ApJ...323..714K.

Keppler, M., M. Benisty, et al. (Sept. 2018). “Discovery of a planetary-mass companion within the gap of the transition disk around PDS 70”. In: *Astronomy & Astrophysics* 617, A44. ISSN: 0004-6361, 1432-0746. DOI: 10.1051/0004-6361/201832957. URL: https://www.aanda.org/10.1051/0004-6361/201832957.

Keppler, M., R. Teague, et al. (May 2019). “Highly structured disk around the planet host PDS 70 revealed by high-angular resolution observations with ALMA”. In: *Astronomy and Astrophysics* 625. ADS Bibcode: 2019A&A...625A.118K, A118. ISSN: 0004-6361. DOI: 10.1051/0004-6361/201935034. URL: https://ui.adsabs.harvard.edu/abs/2019A&A...625A.118K.

Kiefer, F., A. L. des Etangs, et al. (Oct. 2014). “Two families of exocomets in the β Pictoris system”. en. In: *Nature* 514.7523, pp. 462–464. ISSN: 1476-4687. DOI: 10.1038/nature13849. URL: https://www.nature.com/articles/nature13849.

Kiefer, F., A. Lecavelier Des Etangs, et al. (Jan. 2014). “Exocomets in the circumstellar gas disk of HD 172555”. en. In: *Astronomy & Astrophysics* 561, p. L10. ISSN: 0004-6361, 1432-0746. DOI: 10.1051/0004-6361/201323128. URL: http://www.aanda.org/10.1051/0004-6361/201323128.

Kley, W. et al. (Sept. 2012). “Planet-disk interaction and orbital evolution”. In: *Annual Review of Astronomy and Astrophysics* 50.1. arXiv:1203.1184 [astro-ph], pp. 211–249. ISSN: 0066-4146, 1545-4282. DOI: 10.1146/annurev-astro-081811-125523. URL: http://arxiv.org/abs/1203.1184.

Lagrange-Henri, A. M. et al. (May 1989). “The circumstellar gas around beta Pictoris. VIII. Evidence for a clumpy structure of the infalling gas.” In: *Astronomy and Astrophysics* 215. ADS Bibcode: 1989A&A...215L...5L, pp. L5–L8. ISSN: 0004-6361. URL: https://ui.adsabs.harvard.edu/abs/1989A&A...215L...5L.

Lubow, S. H. et al. (Apr. 2012). “ACCRETION OUTBURSTS IN CIRCUMPLANETARY DISKS”. en. In: *The Astrophysical Journal Letters* 749.2, p. L37. ISSN: 2041-8205. DOI: 10.1088/2041-8205/749/2/L37. URL: https://doi.org/10.1088/2041-8205/749/2/L37.

Mayor, M. et al. (Dec. 2003). “Setting New Standards with HARPS”. In: *The Messenger* 114. ADS Bibcode: 2003Msngr.114...20M, pp. 20–24. ISSN: 0722-6691. URL: https://ui.adsabs.harvard.edu/abs/2003Msngr.114...20M.

Müller, A. et al. (Sept. 2018). “Orbital and atmospheric characterization of the planet within the gap of the PDS 70 transition disk”. In: *Astronomy and Astrophysics* 617. ADS Bibcode: 2018A&A...617L...2M, p. L2. ISSN: 0004-6361. DOI: 10.1051/0004-6361/201833584. URL: https://ui.adsabs.harvard.edu/abs/2018A&A...617L...2M.

Novais, A. et al. (July 2025). *Sublimating exocomets in the PDS 70 system*. ISSN: 2693-5015. DOI: 10.21203/rs.3.rs-6925058/v1. URL: https://www.researchsquare.com/article/rs-6925058/v1.

Pecaut, M. J. et al. (Sept. 2016). “The star formation history and accretion-disc fraction among the K-type members of the Scorpius-Centaurus OB association”. In: *Monthly Notices of the Royal Astronomical Society* 461. ADS Bibcode: 2016MNRAS.461..794P, pp. 794–815. ISSN: 0035-8711. DOI: 10.1093/mnras/stw1300. URL: https://ui.adsabs.harvard.edu/abs/2016MNRAS.461..794P.

Perets, H. B. et al. (May 2011). “Wind-shearing in Gaseous Protoplanetary Disks and the Evolution of Binary Planetesimals”. In: *The Astrophysical Journal* 733. ADS Bibcode: 2011ApJ...733...56P, p. 56. ISSN: 0004-637X. DOI: 10.1088/0004-637X/733/1/56. URL: https://ui.adsabs.harvard.edu/abs/2011ApJ...733...56P.

Perotti, G. et al. (Aug. 2023). “Water in the terrestrial planet-forming zone of the PDS 70 disk”. en. In: *Nature* 620.7974, pp. 516–520. ISSN: 0028-0836, 1476-4687. DOI: 10.1038/s41586-023-06317-9. URL: https://www.nature.com/articles/s41586-023-06317-9.

Pinilla, P. et al. (June 2024). “Survival of the long-lived inner disk of PDS70”. In: *Astronomy and Astrophysics* 686. ADS Bibcode: 2024A&A...686A.135P, A135. ISSN: 0004-6361. DOI: 10.1051/0004-6361/202348707. URL: https://ui.adsabs.harvard.edu/abs/2024A&A...686A.135P.

Poincaré, J. H. (Jan. 1890). *Sur le problème des trois corps et les équations de la dynamique*. Vol. 13. Acta Mathematica.

Portilla-Revelo, B. et al. (Sept. 2023). “Constraining the gas distribution in the PDS 70 disc as a method to assess the effect of planet-disc interactions”. In: *Astronomy and Astrophysics* 677. ADS Bibcode: 2023A&A...677A..76P, A76. ISSN: 0004-6361. DOI: 10.1051/0004-6361/202346607. URL: https://ui.adsabs.harvard.edu/abs/2023A&A...677A..76P.

Rappaport, S. et al. (Feb. 2018). “Likely transiting exocomets detected by Kepler”. In: *Monthly Notices of the Royal Astronomical Society* 474. ADS Bibcode: 2018MNRAS.474.1453R, pp. 1453–1468. ISSN: 0035-8711. DOI: 10.1093/mnras/stx2735. URL: https://ui.adsabs.harvard.edu/abs/2018MNRAS.474.1453R.

Rein, H. and S.-F. Liu (Jan. 2012). “REBOUND: An open-source multi-purpose N-body code for collisional dynamics”. In: *Astronomy & Astrophysics* 537. arXiv:1110.4876 [astro-ph], A128. ISSN: 0004-6361, 1432-0746. DOI: 10.1051/0004-6361/201118085. URL: http://arxiv.org/abs/1110.4876.

Rein, H. and D. S. Spiegel (Jan. 2015). “IAS15: a fast, adaptive, high-order integrator for gravitational dynamics, accurate to machine precision over a billion orbits”. In: *Monthly Notices of the Royal Astronomical Society* 446. ADS Bibcode: 2015MNRAS.446.1424R, pp. 1424–1437. ISSN: 0035-8711. DOI: 10.1093/mnras/stu2164. URL: https://ui.adsabs.harvard.edu/abs/2015MNRAS.446.1424R.

Ronnet, T. et al. (Jan. 2020). “Formation of moon systems around giant planets - Capture and ablation of planetesimals as foundation for a pebble accretion scenario”. en. In: *Astronomy & Astrophysics* 633, A93. ISSN: 0004-6361, 1432-0746. DOI: 10.1051/0004-6361/201936804. URL: https://www.aanda.org/articles/aa/abs/2020/01/aa36804-19/aa36804-19.html.

Soichiro Hattori et al. (Mar. 2024). *{{exoplanet-dev/jaxoplanet: Astronomical time series analysis with JAX}}*. DOI: 10.5281/zenodo.10736936. URL: https://doi.org/10.5281/zenodo.10736936.

Stolker, T. et al. (Dec. 2020). “MIRACLES: atmospheric characterization of directly imaged planets and substellar companions at 4–5 μm - II. Constraints on the mass and radius of the enshrouded planet PDS 70 b”. en. In: *Astronomy & Astrophysics* 644, A13. ISSN: 0004-6361, 1432-0746. DOI: 10.1051/0004-6361/202038878. URL: https://www.aanda.org/articles/aa/abs/2020/12/aa38878-20/aa38878-20.html.

Supulver, K. D. et al. (Aug. 2000). “Formation of Icy Planetesimals in a Turbulent Solar Nebula”. In: *Icarus* 146.2, pp. 525–540. ISSN: 0019-1035. DOI: 10.1006/icar.2000.6418. URL: https://www.sciencedirect.com/science/article/pii/S0019103500964182.

Szebehely, V. G. (1967). *Theory of orbits, the restricted problem of three bodies*. eng. New York, Academic Press. URL: http://archive.org/details/theoryoforbitsre0000szeb.

Tamayo, D. et al. (Jan. 2020). “REBOUNDx: a library for adding conservative and dissipative forces to otherwise symplectic N-body integrations”. In: *Monthly Notices of the Royal Astronomical Society* 491.2, pp. 2885–2901. ISSN: 0035-8711. DOI: 10.1093/mnras/stz2870. URL: https://doi.org/10.1093/mnras/stz2870.

Thanathibodee, T. et al. (Apr. 2020). “Variable Accretion onto Protoplanet Host Star PDS 70”. In: *The Astrophysical Journal* 892. ADS Bibcode: 2020ApJ...892...81T, p. 81. ISSN: 0004-637X. DOI: 10.3847/1538-4357/ab77c1. URL: https://ui.adsabs.harvard.edu/abs/2020ApJ...892...81T.

Toci, C. et al. (Oct. 2020). “Planet migration, resonant locking, and accretion streams in PDS 70: comparing models and data”. en. In: *Monthly Notices of the Royal Astronomical Society* 499.2, pp. 2015–2027. ISSN: 0035-8711, 1365-2966. DOI: 10.1093/mnras/staa2933. URL: https://academic.oup.com/mnras/article/499/2/2015/5911603.

Trevascus, D. et al. (Apr. 2025). *Differentiating Formation Models with New Dynamical Masses for the PDS 70 Protoplanets*. arXiv:2504.11210 [astro-ph]. DOI: 10.48550/arXiv.2504.11210. URL: http://arxiv.org/abs/2504.11210.

Vicente, S. M. et al. (Oct. 2005). “Size distribution of circumstellar disks in the Trapezium cluster”. In: *Astronomy and Astrophysics* 441. ADS Bibcode: 2005A&A...441..195V, pp. 195–205. ISSN: 0004-6361. DOI: 10.1051/0004-6361:20053540. URL: https://ui.adsabs.harvard.edu/abs/2005A&A...441..195V.

Wagner, W. et al. (May 1993). “International Equations for the Saturation Properties of Ordinary Water Substance. Revised According to the International Temperature Scale of 1990. Addendum to J. Phys. Chem. Ref. Data 16, 893 (1987)”. In: *Journal of Physical and Chemical Reference Data* 22.3, pp. 783–787. ISSN: 0047-2689. DOI: 10.1063/1.555926. URL: https://doi.org/10.1063/1.555926.

Wallace, S. C. et al. (Apr. 2021). “Collision rates of planetesimals near mean-motion resonances”. en. In: *Monthly Notices of the Royal Astronomical Society* 503.4, pp. 5409–5424. ISSN: 0035-8711, 1365-2966. DOI: 10.1093/mnras/stab792. URL: https://academic.oup.com/mnras/article/503/4/5409/6178856.

Wang, J. J. et al. (Mar. 2021). “Constraining the Nature of the PDS 70 Protoplanets with VLTI/GRAVITY”. In: *The Astronomical Journal* 161. ADS Bibcode: 2021AJ....161..148W, p. 148. ISSN: 0004-6256. DOI: 10.3847/1538-3881/abdb2d. URL: https://ui.adsabs.harvard.edu/abs/2021AJ....161..148W.

Whipple, F. L. (Mar. 1950). “A comet model. I. The acceleration of Comet Encke”. In: *The Astrophysical Journal* 111. ADS Bibcode: 1950ApJ...111..375W, pp. 375–394. ISSN: 0004-637X. DOI: 10.1086/145272. URL: https://ui.adsabs.harvard.edu/abs/1950ApJ...111..375W.

Williams, J. P. et al. (Sept. 2011). “Protoplanetary Disks and Their Evolution”. In: *Annual Review of Astronomy and Astrophysics* 49. ADS Bibcode: 2011ARA&A..49...67W, pp. 67–117. ISSN: 0066-4146. DOI: 10.1146/annurev-astro-081710-102548. URL: https://ui.adsabs.harvard.edu/abs/2011ARA&A..49...67W.

Youdin, A. N. et al. (Feb. 2005). “Streaming Instabilities in Protoplanetary Disks”. In: *The Astrophysical Journal* 620. ADS Bibcode: 2005ApJ...620..459Y, pp. 459–469. ISSN: 0004-637X. DOI: 10.1086/426895. URL: https://ui.adsabs.harvard.edu/abs/2005ApJ...620..459Y.

Zieba, S. et al. (May 2019). “Transiting exocomets detected in broadband light by TESS in the β Pictoris system”. en. In: *Astronomy & Astrophysics* 625, p. L13. ISSN: 0004-6361, 1432-0746. DOI: 10.1051/0004-6361/201935552. URL: https://www.aanda.org/articles/aa/abs/2019/05/aa35552-19/aa35552-19.html.